ACS OMEGA

Open Access

http://pubs.acs.org/journal/acsodf

Review

Recent Advances of Indium-Based Sulfides in Photocatalytic CO_2 Reduction

Hongyan Zhang and Qian Su*

Cite This: *ACS Omega* 2025, 10, 8793−8815

Read Online

ACCESS | Metrics & More | Article Recommendations

ABSTRACT: Urgent and significant, the mitigation of greenhouse effects and the preservation of the Earth's ecological environment are paramount concerns. Photocatalytic carbon dioxide (CO_2) reduction technology holds immense promise as it directly harnesses renewable solar energy to convert CO_2 into hydrocarbon fuels and valuable chemical products. Indium (In)-based sulfides have garnered significant attention in the realm of fundamental research on CO_2 photocatalytic conversion. The photocatalytic performance exhibited by In-based materials is attributed to the appropriate bandgap (E_g), unique electronic states, tunable atomic structure, and superior optoelectronic properties. Notably, In-based metal sulfides also show excellent potential for addressing challenges related to photocorrosion and carrier recombination. This paper highlighted the key structural features and commonly employed synthesis techniques of In-based metal sulfides. Furthermore, it summarized effective modification strategies aimed at optimizing the photocatalytic performance of these materials. A particular focus was placed on exploring the intricate structure−activity relationships, encompassing the influence of heterostructure construction, element doping, defect engineering, and co-catalyst modification on enhancing photocatalytic efficiency. Finally, the article identified the current challenges and outlined the promising future directions for In-based photocatalysts, hoping to provide valuable references for researchers.

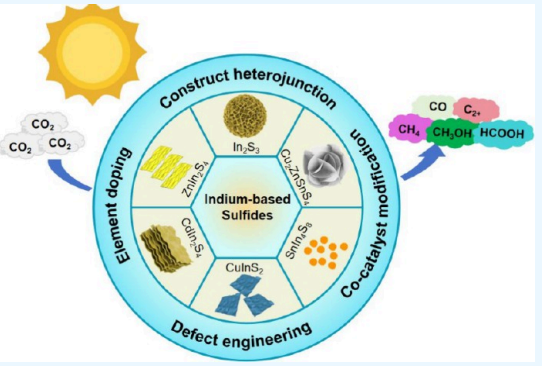

1. INTRODUCTION

Under the severe challenges of current environmental pollution and energy crisis, the significance of environmental management is increasingly prominent. Human beings' excessive reliance on nonrenewable fossil fuels has led to excessive carbon dioxide emissions, disrupting the carbon cycle.[1−3] Addressing energy and environmental challenges requires advanced technologies to balance production and sustainability. The rapid growth of the new energy industry offers opportunities to reduce carbon pollution, among which photocatalytic technology has attracted extensive attention due to its characteristic of directly utilizing solar energy.[4−8]

Since Inoue et al.[9] reported the phenomenon of semiconductor photocatalytic reduction of carbon dioxide in 1979, this research field has evolved from the stage of exploring fundamental mechanisms to the stage of innovating material systems. Recent studies show that TiO_2-based materials exhibit a quantum efficiency of approximately 8% in the ultraviolet region, but their wide bandgap characteristics (about 3.2 eV) severely limit the utilization efficiency of visible light.[10−12] This limiting factor has promoted the development of narrow bandgap semiconductor materials (such as WO_3,[13] $BiVO_4$,[14] CdSe,[15] Ta_3N_5,[16] C_3N_4,[17] etc.). For instance, Cu_2O (with a bandgap of about 2.0 eV) has seen a 24-fold increase in the efficiency of photocatalytic CO_2 reduction to CO (13.4 μmol·cm^{-2} h^{-1}) through the design of a three-dimensional porous structure.[18] g-C_3N_4 nanotubes (with a bandgap of about 2.7 eV) have seen their CO_2 conversion rate increase to 103.6 μmol·g^{-1} h^{-1} through amino modification.[19] Despite this, these materials still face the problem of high carrier recombination rates.[20] Compared with metal oxides, metal sulfides have narrower bandgaps (1.2−2.4 eV) and a wider range of light response.[21−25] Taking the typical metal sulfide system as an example, MoS_2, by constructing a 1*T*/2H heterojunction, has a significantly higher light absorption intensity in the 200−800 nm range than 1T-MoS_2 and 2H-MoS_2.[26] WS_2 nanosheets can extend the light response to the visible and even near-infrared regions.[27] However, these single-metal sulfides generally suffer from photodegradation problems,[28] with their activity decreasing by more than 60% after continuous light exposure for 12 h.[26]

Received: October 17, 2024
Revised: February 13, 2025
Accepted: February 14, 2025
Published: February 26, 2025

https://doi.org/10.1021/acsomega.4c09487
ACS Omega 2025, 10, 8793−8815

In-based sulfides form a unique electronic structure by hybridizing the 5s orbital of In^{3+} with the 3p orbital of S.[29] In recent years, In-based metal sulfides (such as In_2S_3, $ZnIn_2S_4$, $CdIn_2S_4$, $CuInS_2$, etc.) have been widely applied in photocatalytic CO_2 conversion. For instance, by controlling the coordination of different sulfur sources to prepare $ZnIn_2S_4$ with appropriate Zn vacancies, the optimized $L_{0.25}T_{0.75}$-ZIS exhibits the best CO generation rate (5.63 $mmol{\cdot}g^{-1}$ h^{-1}) under visible light, with a selectivity of 97.9%.[30] $CuInS_2$ (with a band gap of 1.52 eV) shows significant visible light absorption ability in the wavelength range of 550 to 800 nm. After use, the crystal structure, chemical composition, and valence state of elements of $CuInS_2$ remain highly consistent with those of fresh samples, indicating its excellent stability.[31] By inducing the formation of an intermediate band through InCu antisite defects in $CuInS_2$, the cascade sub-band transitions of high-energy and low-energy photons can be achieved, significantly enhancing the absorption range of infrared light and the utilization efficiency of photogenerated carriers. Under full-spectrum irradiation, the CO production rate of $CuInS_2$ reaches 19.9 $\mu mol{\cdot}g^{-1}$ h^{-1}, which is more than seven times that under UV−visible light irradiation alone.[32] Despite these advancements, In-based sulfides still face some challenges in the photocatalytic CO_2 reduction process. The regulation mechanism of reaction pathways and long-term stability (>200 h) remain bottlenecks for industrial applications.[33,34]

In conclusion, In-based sulfides demonstrate great potential for application in the field of photocatalytic CO_2 reduction. However, further research is still needed to enhance their performance and stability. Researchers have carried out numerous studies, including the design of the structure of In-based sulfides, surface modification, and construction of composite materials. This review will systematically summarize the research progress of In-based sulfides in the field of photocatalytic CO_2 reduction, including their structural characteristics, synthesis methods, modification strategies, and mechanisms for improving catalytic performance, in order to provide a reference for the research in this field. At the same time, it will deeply explore the problems and challenges existing in the photocatalytic CO_2 reduction process of In-based sulfides, and look forward to the future development direction, in order to promote the further development and application of In-based sulfide photocatalytic materials.

2. PHOTOCATALYTIC REACTION

2.1. Principle of Photocatalytic CO_2 Reduction Reaction. Photocatalytic CO_2 reduction technology mimics natural photosynthesis, using solar energy to drive the conversion of CO_2 and H_2O into fuels (such as CO, CH_4) or high value-added chemicals (such as formic acid, methanol).[35,36] This process is realized by photocatalyst, the core of which is the absorption and conversion of light energy by semiconductor materials. When a semiconductor absorbs photons with energy greater than its forbidden band gap (E_g), the electrons in the valence band (VB) are excited to transition to the conduction band (CB), forming an electron−hole pair (e^-−h^+), which provides the driving force for the subsequent reaction (Figure 1).[37] The design of the band structure is crucial: the negative conduction potential needs to be sufficient to reduce CO_2, while the positive valence band needs to meet the oxidation demand of H_2O.[38,39] This potential matching

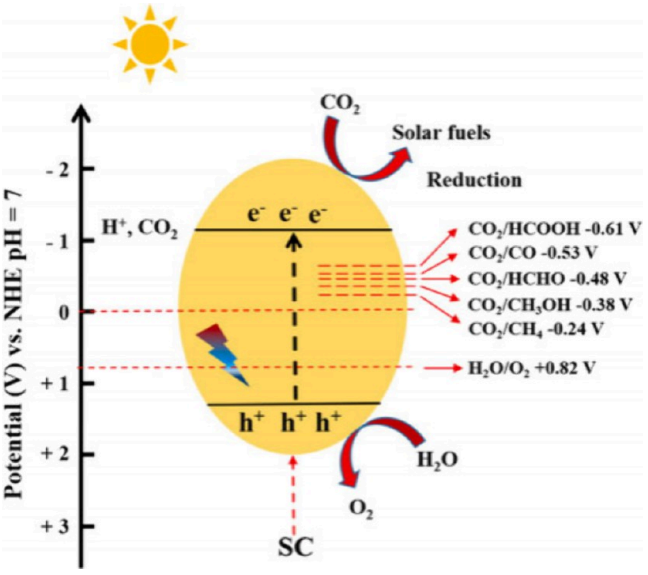

Figure 1. Mechanism of photocatalytic CO_2 reduction. Reprinted with permission from ref 37. Copyright 2022, Elsevier.

directly determines whether the reaction can be carried out efficiently.

The photocatalytic reaction consists of three continuous stages: light energy capture and carrier generation, carrier separation and migration, and surface redox reaction. In the light energy capture stage, the semiconductor absorbs specific wavelengths of light (such as ultraviolet or visible light) to produce e^-−h^+ pairs; Subsequently, electrons and holes need to be rapidly separated and migrated to the photocatalyst surface.[40] If they are combined in the migration process, it will lead to energy loss and significantly reduce the reaction efficiency. The carriers that reach the surface participate in redox reactions. Photogenerated electrons reduce adsorbed CO_2 to CO or hydrocarbons, while holes oxidize H_2O to produce oxygen and protons, which further participate in the reduction process. The whole process requires the photocatalyst not only to have a suitable light absorption capacity, but also to provide an efficient charge transport path and rich surface active sites.[41]

However, the technology still faces multiple challenges. First of all, the recombination rate of electron−hole pairs is high, which limits the efficiency of light energy conversion. Photogenerated carriers separation should be promoted by constructing heterojunction or introducing defect engineering. Second, most semiconductors (such as TiO_2) only absorb ultraviolet light, the utilization of the solar spectrum is insufficient, and the light response range can be broadened by element doping or loading co-catalyst.[42] In addition, the adsorption capacity of CO_2 molecules on the catalyst surface is weak, resulting in low activation efficiency, and the design of large specific surface area or the introduction of active sites can enhance its adsorption and activation. Another key issue is reaction selectivity, where holes may oxidize the resulting reduction products, and hole trapping agents or spatial isolation strategies need to be developed to inhibit side reactions.[43] Despite the challenges, photocatalytic CO_2 reduction technology shows great potential in the field of carbon cycling and energy conversion. By optimizing semiconductor band structure, interfacial charge transport mechanism, and surface catalytic active sites, this technology is

https://doi.org/10.1021/acsomega.4c09487
ACS Omega 2025, 10, 8793−8815

expected to achieve efficient conversion of solar energy to chemical energy.

2.2. Current Status of Research on Photocatalytic CO_2 Reduction Reaction. The research background of photocatalytic CO_2 reduction can be traced back to the early 1970s, when the use of semiconductor materials to convert solar energy into chemical energy was first explored. The discovery of photocatalytic decomposition of water to produce hydrogen and oxygen using semiconductor materials such as titanium dioxide (TiO_2) laid the foundation for subsequent CO_2 reduction research.[44] Nowadays, photocatalytic CO_2 reduction has emerged as a potential method to address the problem of climate change and the surging demand for renewable energy. Photocatalytic reduction of CO_2 has a promising application in the field of renewable energy and environmental protection. This method is proposed to use sunlight as energy for the efficient conversion of CO_2. When light is excited, the photocatalytic material effectively absorbs sunlight and generates photons and holes. The effective separation of photogenerated electrons and holes is achieved by utilizing the built-in electric field of the semiconductor. The photogenerated electrons can be absorbed and transferred to the CB with higher energy level, while the oxidized holes are retained in the VB. Photogenerated electrons can participate in the catalytic reduction of CO_2 and convert it into various products such as CO and hydrocarbons. The holes remaining in the valence band are highly reactive and can participate in side reactions leading to a reduction in overall efficiency. Therefore, introducing a sacrificial agent into the system to react with the photogenerated holes prevents unwanted side reactions from occurring, reduces electron−hole complexation, and avoids reoxidation of the photogenerated electrons by the generated holes or by the oxygen generated in the water. Common sacrificial agents include alcohols or other easily oxidized compounds (e.g., H_2O_2, Na_2SO_3/Na_2S, CH_3OH and triethanolamine).

In the process of photocatalytic reduction of CO_2, the photocatalyst serves as the pivotal component, significantly influencing not just the conversion efficiency of CO_2, but also determining the yield and selectivity of the desired product. Among the commonly utilized photocatalysts are metal oxides, composite metal oxides, metal sulfides, polymers, mesoporous materials, and metal−organic frameworks (MOFs). These photocatalysts generate photoexcited charge carriers that participate in redox reactions, facilitating the reduction of CO_2 to CO and other compounds under various catalytic conditions. Furthermore, in certain scenarios, protons (H^+) derived from water or other sources can be reduced along with CO_2, leading to the formation of reduction products such as HCOOH, CH_3OH, or other high-value hydrocarbons.[45,46]

3. In-BASED METAL SULFIDES

3.1. Characteristics of Metal Sulfides. Metal sulfides are compounds that arise from the bonding of a negative sulfur ion with one or more metal cations. Within these compounds, the S 3p orbital assumes a positive valence band position and possesses a small effective mass carrier. This unique configuration grants metal sulfides exceptional properties, including a favorable energy band structure, a broad spectral response range, and rapid charge carrier dynamics. Depending on the type of metal ions involved, metal sulfides can be categorized into various groups: binary metal sulfides (such as CdS and In_2S_3), ternary metal sulfides (such as $ZnIn_2S_4$ and $CdIn_2S_4$), and quaternary metal sulfides (such as Cu_2ZnSnS_4). These compounds exhibit an optimal energy band structure, resulting in strong absorption of visible light and superior redox properties. Additionally, metal sulfides display high structural symmetry and impressive photogenerated charge transport rates, characteristics that render them potentially valuable for photocatalysis applications. However, there remains a significant performance gap between metal sulfides and their practical needs. Notably, the energy band structure of semiconductor materials plays a pivotal role in determining their photocatalytic performance. Therefore, optimizing the energy band structure of metal sulfides is expected to further enhance their photocatalytic performance and foster their development in practical applications.

3.2. Classification of In-Based Sulfides. *3.2.1. Binary In-Based Sulfides.* Binary metal sulfides are a class of compounds composed of metal elements and sulfur elements. They have the advantages of simple structure, easy synthesis, and excellent performance.[47] Binary In-based sulfides are mainly represented by In_2S_3, which is an n-type semiconductor and exists in three different phases: α, β, and γ. Among them, β-In_2S_3 has attracted considerable attention due to its narrow bandgap (2.0−2.3 eV), high stability, and high absorbance in the visible light region.[48] Due to its ease of synthesis, excellent stability, and relatively low toxicity, In_2S_3 has become a preferred material for photocatalytic applications. However, the photocatalytic efficiency of In_2S_3 is limited by the easy recombination of charge carriers. Moreover, photocatalytic redox reactions involve multiple complex processes, including adsorption/desorption, the generation of photoexcitation, the recombination and transfer of electrons and holes, the presence of active surface products/reactants, mass transfer rates, and stability. Single-component photocatalysts often fail to meet the requirements of both stability and wide light absorption ability, making it difficult to optimize all these processes simultaneously. To enhance the photocatalytic activity of In_2S_3, researchers have considered combining it with other narrow bandgap materials to form composite materials. These composites can be further combined with other visible light-active materials or carbonaceous materials with high conductivity to further improve their photocatalytic performance.

Miao et al.[48] successfully synthesized a novel flower-like β-In_2S_3/NiAl-LDH photocatalyst using one-step hydrothermal method. Under simulated solar light irradiation, the In_2S_3/LDH composite exhibited remarkable photocatalytic performance and stability in the photocatalytic reduction of CO_2 in water. The experimental results revealed that the 30% In_2S_3/NiAl-LDH photocatalyst demonstrated superior photocatalytic activity. After irradiation with visible light for 7 h, the maximum yield of CH_4 reached 36.1 $\mu mol \cdot g_{cat}^{-1}\ h^{-1}$, which exceeded that of LDH and undoped In_2S_3 by factors of 2.5 and 3.5, respectively. The outstanding photocatalytic performance of 30% In_2S_3/NiAl-LDH can be attributed to several factors: (i) the formation of a type-II heterojunction effectively promotes the separation of charge carriers and suppresses their recombination; (ii) the uniform dispersion of In_2S_3 on the LDH surface significantly enhances the specific surface area of the composite material; (iii) the incorporation of In_2S_3 augments the visible light absorption capacity. Similarly, Abdulrahman et al.[49] prepared an In_2S_3/WS_2 (InS/WS) type-II heterostructure using a hydrothermal method (Figure 2). Compared to pure In_2S_3 and WS_2, the InS/WS material

https://doi.org/10.1021/acsomega.4c09487
ACS Omega 2025, 10, 8793−8815

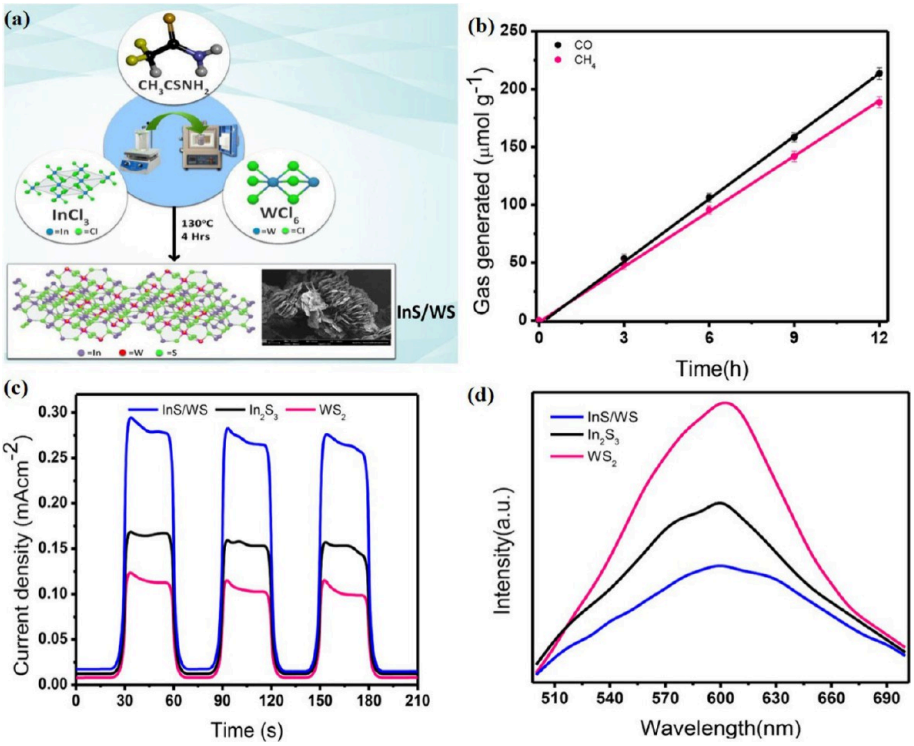

Figure 2. (a) Synthesis of InS/WS heterostructures, (b) efficiency of producing CO and CH_4 with InS/WS heterostructure under visible light, (c) transient photocurrent response and (d) PL spectra of In_2S_3, WS_2 and InS/WS heterostructure. Reprinted with permission from ref 49. Copyright 2023, Elsevier.

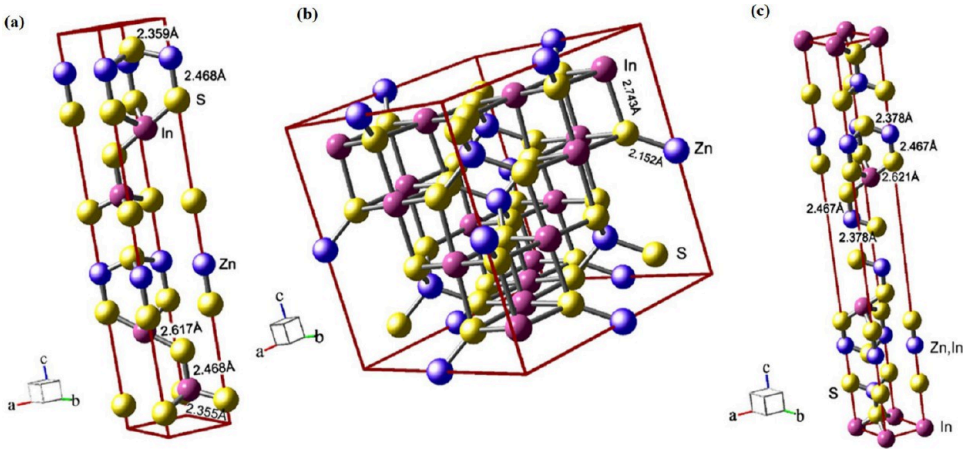

Figure 3. Crystal structures of (a) hexagonal, (b) cubic and (c) rhombic $ZnIn_2S_4$. Reprinted with permission from ref 51. Copyright 2011, Elsevier.

exhibited superior photocatalytic activity. Under visible light, the photocatalyst reduced CO_2 to produce 213.4 μmol of CO and 188.6 μmol of CH_4 after 12 h of reaction. The improvement in photocatalytic CO_2 reduction performance is mainly attributed to the formation of a type II heterojunction and the layered structure that facilitates electron mobility. This structure facilitates the effective separation of charges, thereby reducing their recombination rate and improving the utilization efficiency of photogenerated carriers. Therefore, the InS/WS heterostructure exhibits excellent activity in the photocatalytic process. Yan et al.[50] used metal−organic frameworks (MOFs) as raw materials and synthesized a series of In_2O/In_2S_3 core−shell heterostructures through a two-step solvothermal method with the addition of different amounts of sulfur-containing reagents (L-cysteine, L-Cys). These heterostructures were then used as photocatalysts for the reduction of CO_2 by water vapor. After illumination, the optimized 1.2-In_2O_3/In_2S_3 sample with the appropriate amount of L-Cys added exhibited the highest yield of CH_4 (14.3 $\mu mol \cdot g_{cat}^{-1}$ h^{-1}) and CO (2.59 $\mu mol \cdot g_{cat}^{-1}$ h^{-1}). Characterization results indicated that the shell structure of the In_2O_3/In_2S_3 photocatalyst significantly improved the separation efficiency of photogenerated carriers and the ability to capture visible light, thereby promoting the photoreduction of CO_2. However, the excessive addition of sulfur-containing reagents disrupted the shell structure, transforming it into a thicker layer of In_2S crystals. This change not only reduced the number of heterostructures but also hindered the adsorption of CO_2 on the reaction surface.

https://doi.org/10.1021/acsomega.4c09487
ACS Omega 2025, 10, 8793−8815

3.2.2. Ternary In-Based Sulfides. Although binary metal sulfides have made significant progress in recent years, their defects such as susceptibility to photocorrosion and single component have restricted their practical applications. However, ternary metal sulfides have attracted much attention due to their high light absorption, carrier migration rate, adjustable composition and energy band. Ternary In-based sulfides are composed of metal elements, indium elements, and sulfur elements, such as $ZnIn_2S_4$, $CdIn_2S_4$, $CuInS_2$, $AgInS_2$, $SnIn_4S_8$. These compounds show broad application prospects in CO_2 reduction reactions and have important potential value.

Ternary $ZnIn_2S_4$ (ZIS) is a commonly used In-based metal sulfide that has been extensively studied due to its better thermal stability in the environment. The crystal phase structures of $ZnIn_2S_4$ mainly include cubic, hexagonal, and rhombohedral, all of which originate from different atomic packing arrangements (Figure 3). Shen et al.[51] explored the photoluminescence properties and photocatalytic activity of $ZnIn_2S_4$ in cubic and hexagonal crystal systems. This research group prepared $ZnIn_2S_4$ samples at different temperatures through the thermal sulfuration method and found that the sulfidation temperature affected its crystal structure. At 300 °C, it remained as an oxide precursor, formed a cubic phase at 400 °C, and a hexagonal phase at 800 °C. $ZnIn_2S_4$ with different crystal structures exhibited different carrier dynamics, which directly affected its photocatalytic performance. $ZnIn_2S_4$ with a cubic structure (such as $ZnIn_2S_4$-400) showed strong photoluminescence quenching, indicating that nonradiative transitions dominated, leading to a reduction in the number of electrons and holes participating in the photocatalytic reaction, thereby reducing photocatalytic activity. As the sulfidation temperature increased, the crystal structure changed from cubic to hexagonal. For example, in samples from $ZnIn_2S_4$-500 to $ZnIn_2S_4$-700, the efficiency of nonradiative transitions decreased, and the emission intensity increased, which meant that the number of electrons and holes available for photocatalytic reactions increased. Therefore, changes in the crystal structure affected the generation and recombination rates of charge carriers, further influencing photocatalytic efficiency. In another study, Chen et al.[52] prepared two $ZnIn_2S_4$ samples with different crystal phase structures through a liquid ultrasonic exfoliation method. According to density functional theory (DFT) calculations, the valence bands of both structures were mainly contributed by Zn 3d orbitals and S 3p orbitals, while the conduction bands were mainly composed of In 5s and 5p orbitals and S 3p orbitals. However, the band gap of hexagonal $ZnIn_2S_4$ was only 0.28 eV, narrower than the 1.36 eV of the cubic structure, making it able to absorb a broader range of spectra and exhibiting superior photocatalytic activity.

Furthermore, $ZnIn_2S_4$ possesses numerous advantageous properties, including low toxicity, tunable bandgap width ranging from 2.2 to 2.6 eV, excellent visible light responsiveness, and remarkable photostability. Wang et al.[53] holds the view that the ZIS/In_2O_3 heterojunction stands out as an ideal catalyst for solar-driven CO_2 reduction and water oxidation reactions. The construction of this composite catalyst combines the advantages of the large specific surface area of In_2O_3 hollow nanotubes and the high light absorption of ZIS, resulting in a CO generation rate of 3075 $\mu mol \cdot g^{-1}$ h^{-1}. Additionally, Xia et al.[54] successfully grew ZIS on N-doped graphene foam in situ using a straightforward hydrothermal method. By harnessing the three-dimensional network structure and exceptional CO_2 adsorption capacity of the graphene foam network, they achieved a photothermal reduction efficiency that exceeded that of pure indium-zinc sulfide by a factor of 5.9.

$CdIn_2S_4$, as one of the important members of the A^{II}-B_2^{III}-C_4^{IV} series of materials, possesses remarkable cubic crystal structure features. The space group to which it belongs is Fd3m and the point group is m3m. The S atoms form chemical bonds with In and Cd atoms, respectively, so that the tetrahedral InS_4 and octahedral CdS_6 microcells together build the overall structure of $CdIn_2S_4$.[55] In addition, the crystal cell of $CdIn_2S_4$ consists of three elements, Cd, In, and S, and its lattice constant is precisely 7.80, which further reveals its unique crystal structure properties. In addition, as a typical n-type semiconductor material with a suitable bandgap (~2.2 eV) and an ideal conduction band position, $CdIn_2S_4$ has been widely reported for its applications in various fields, such as photocatalytic hydrogenation precipitation, photocatalytic degradation of organic pollutants, and photocatalytic CO_2 conversion. However, due to their slow photogenerated carrier separation and lack of catalytically active sites, they are still facing the challenge of making significant breakthroughs in catalytic activity. Li et al.[56] prepared bimetallic Ce/Zr-UiO-66-NH_2/$CdIn_2S_4$ heterojunctions with different Ce contents by a solvothermal method. The CO_2 reduction performance of the catalyst was investigated under simulated solar irradiation without adding any sacrificial agent. The optimized 8-$Ce_{0.2}$NU66/CIS (Zr/Ce = 1/0.2) photocatalytic CO_2 reduction rate was 6.01 $\mu mol \cdot g^{-1}$ h^{-1}, which was 3.72 times higher than that of pristine $CdIn_2S_4$ and 17.83 times higher than that of MOF, respectively. The characterization results indicate that doping Ce ions can generate some oxygen vacancies (OVs) and increase the electron density around Zr^{4+} ions, which ultimately improves the photocatalytic effect, while the presence of heterojunction interfaces enhances the material's charge transfer capability. This research provides design ideas for the construction of mixed-valence bimetallic MOFs for solar-driven CO_2 conversion.

The ternary quantum dot material $AgInS_2$ (AIS), a semiconductor from the I-III-VI group, exhibits a high extinction coefficient and exceptional optical characteristics in the visible to near-infrared spectrum. It has progressively supplanted cadmium-containing quantum dots in the realms of biomedicine and photonics.[57] Nevertheless, its relatively narrow band gap (~1.8 eV) leads to an excessively rapid recombination rate of photoexcited electron−hole pairs, and the propensity of polymetallic sulfide quantum dots to aggregate and undergo photocorrosion hampers enhancements in photocatalytic efficiency. Wang et al.[58] discovered that the AIS QDs-MoS_2/Go (AIS-MS/GO) composite significantly enhances the photocatalytic degradation of tetracycline (TC) and the photoreduction of CO_2. In comparison to AIS and layered MoS_2, these composite heterojunction photocatalysts adeptly address the aggregation and photoetching issues of AIS and layered MoS_2, establishing a comprehensive electron transport system via the interface coupling of the ternary system, which markedly enhances the mobility and separation efficiency of photogenerated carriers. Notably, when employing AIS-MS/GO-8 composites, the yields of CO and CH_4 reached 52.6 and 28.5 $\mu mol \cdot g^{-1}$, respectively. Although the selectivity for CH_4 is merely 35.1%, this study offers a novel perspective for the rational design of heterojunction-based photocatalysts, with performance enhancements achieved

https://doi.org/10.1021/acsomega.4c09487
ACS Omega 2025, 10, 8793−8815

Table 1. Evaluation of Photocatalytic CO_2 Reduction Performance of Different Catalytic Systems

Photocatalyst	Solution	Light source	Product	Yield (μmol·g^{-1} h^{-1})	Ref.
$Zn_{0.5}Cd_{0.5}S/MoTe_2$	H_2O	300 W Xe lamp	CO	71.79	67
PO_4^{3-}-TiO_2-Ag_x	H_2O	300 W Xe lamp	CO	0.69	68
			CH_4	3.36	
$In_2O_3/Bi_{19}Br_3S_{27}$	$NaSO_3$	300 W Xe lamp	CO	28.36	69
Bi/TiO_2	H_2O	300 W Xe lamp	CO	36.7	70
			CH_4	60.2	
Cu^ICo^{II}-$(N^SN^N)_m$	TEOA[a]	Blue LED visible light	CO	0.38	71
MIL-88B-NS40	H_2O	300 W Xe lamp	CO	676.5	72
$Co/g\text{-}C_3N_4$	H_2O	300 W Xe lamp	CO	2.9	73
			CH_4	3.4	
$In_2S_3/CuInS_2$	$NaSO_3$	300 W Xe lamp	CO	80.3	74
			CH_4	11.8	
$WO_3/ZnIn_2S_4$	H_2O	300 W Xe lamp	CO	51.3	75
			CH_4	58.7	

[a]TEOA: triethanolamine.

through interface control strategies. Deng et al.[59] engineered and synthesized a novel quantum dot catalyst, polyethylenimine (PEI)-coated silver indium sulfur quantum dots ($AgInS_2$@PEI QDs), tailored for the photocatalytic reduction of CO_2 to C_2H_6. It was observed that the yield and selectivity of C_2H_6 could be notably enhanced by modulating the silver (Ag) and PEI content within the $AgInS_2$@PEI QDs. Under optimal conditions, the yield of C_2H_6 can attain 63 μmol·g^{-1}, with an electronic selectivity of 30.3%. Furthermore, the study indicated that the Ag content plays a pivotal role in the selectivity of C_2H_6. The presence of Ag fosters the C−C coupling reaction at asymmetric bimetallic sites by intensifying the local CO enrichment environment. By harmonizing the generation and consumption rates of *CO intermediates, the selectivity of C_2H_6 is optimized. This work furnishes new insights for the design of efficient quantum dot photocatalysts aimed at converting CO_2 into C_2 products.

$SnIn_4S_8$ stands out as a typical n-type bimetallic sulfide semiconductor, characterized by its unique cubic spinel architecture. The semiconductor's narrow bandgap, coupled with its adjustable electronic and optical attributes, positions $SnIn_4S_8$ as a leading candidate for utilization in solar cells and photocatalytic processes. Comparable to a multitude of photocatalysts that respond to visible light, $SnIn_4S_8$ exhibits superior solar energy conversion efficiency and quantum yield, a consequence of its narrow bandgap. Nonetheless, akin to numerous other photocatalysts with narrow bandgaps, the high rate of photoluminescent electron−hole recombination poses a constraint on its photocatalytic efficacy.[60,61] To address this challenge, scholars have explored diverse methodologies, such as the enhancement of $SnIn_4S_8$ by incorporating additional semiconductors or nanomaterials, including carbon nanotubes, graphene, metal oxides, and metal sulfides, making some progress in enhancing its photocatalytic properties.[62−64]

3.2.3. Quaternary In-Based Sulfides. Currently, quaternary solid solutions have been developed as solar absorbers or photocatalysts due to their adjustable band gap, which can greatly improve their performance. For example, Cu-In-Zn-S, Ag-In-Ga-S, Ag-In-Zn-S, etc. As a new type of Quaternary quantum dots, Cu-In-Zn-S (CIZS) has the characteristics of non toxicity, controllable band gap and suitable redox potential. CIZS can effectively reduce the carrier recombination rate and has significant energy conversion efficiency in the visible and near-infrared regions. CIZS QDs are evenly covered on the surface of hollow CN, which retains the excellent visible light absorption characteristics of quantum dots and improves the separation efficiency of photogenerated carriers.[65] In addition, by adjusting the composition of metal cation precursors (such as zinc, copper or indium ions) in quaternary indium-based sulfide materials, the energy band level can be adjusted to enhance the photocatalytic activity. For example, by combining $AgInS_2$ with a band gap of 1.8 eV and ZnS with a band gap of 3.5 eV, the $(AgIn)_{0.22}Zn_{1.56}S_2$ with a band gap of about 2.3 eV was synthesized, which is conducive to photocatalytic reaction.[66] Therefore, the design and synthesis of new quaternary solid solutions with adjustable energy structure and band gap is one of the most effective ways to develop new photocatalysts or light absorbers with better performance.

Among the numerous candidates for photocatalysts, In-based sulfide stands out as one of the most promising materials for photocatalytic CO_2 reduction, owing to its exceptional properties (Table 1).[67−75] In-based sulfides exhibit a wide light absorption range and unique bimetallic site properties, which provide significant advantages for their applications in the field of CO_2 conversion. The unique bimetallic structure of the material gives it a wealth of active sites, which can effectively regulate the adsorption and desorption processes of key intermediates, thereby improving the CO_2 reactivity and precisely controlling the selectivity of the target product. Compared with monometallic sulfide, In-based sulfide shows better stability due to the increase of metal types. In addition, In-based sulfides have suitable band structure and excellent carrier transport performance, which helps to promote the rapid electron migration in the photocatalytic CO_2 reduction reaction.[59] In recent decades, researchers have conducted in-depth research on the synthesis methods of In-based sulfides and successfully constructed multiple forms by considering multiple factors and regulatory parameters. In a typical photocatalytic CO_2 reduction process, In-based sulfides can rapidly separate photogenerated electron−hole pairs when excited by visible light, and transfer electrons and holes to CB and VB, respectively. Subsequently, photocarriers migrate to the surface of In-based sulfides, triggering the CO_2 reduction reaction and its corresponding oxidation reaction. However, this process is accompanied by significant electron reflux and hole recombination problems. Although the relatively narrow band gap of indium sulfide is favorable for light absorption, the

https://doi.org/10.1021/acsomega.4c09487
ACS Omega 2025, 10, 8793−8815

carrier recombination problem has become a major obstacle to the improvement of catalyst performance.[62] Therefore, many modification strategies have been applied to In-based sulfides. Extensive adjustment of catalyst morphology and crystal structure is carried out to effectively improve the light absorption performance of the material, enhance the adsorption site, and control the transport distance of electrons from the interior to the surface. In addition, on the premise of ensuring that the light capture capacity is sufficient to meet the smooth process of CO_2 light conversion, the energy band structure can be adjusted by molecular regulatory means such as doping and vacancy construction to promote charge separation. The combination of In-based sulfides with other semiconductor materials to form various effective heterostructures is also one of the widely studied methods to improve carrier behavior. A variety of modification strategies, including those described above, have been applied to the modification of In-based sulfides to achieve performance breakthroughs and achieve encouraging results.

4. SYNTHESIS METHODS OF In-BASED METAL SULFIDES

The synthesis of In-based metal sulfides primarily falls into three categories: solid-phase, gas-phase, and liquid-phase methods. Solid-phase techniques, despite their high yield, are often associated with significant energy consumption, particularly when employing high-temperature and high-pressure methods, as well as limited purity in cases where grinding methods are used. In gas-phase synthesis, all reaction components exist in the gaseous state, and the target products are subsequently condensed into solid particles. Achieving high purity in this process necessitates rigorous control of reaction conditions, particularly regarding the atmosphere and temperature. Consequently, gas-phase methods are not typically favored in laboratory settings. Similarly, solid-phase methods are also not widely used due to their inherent limitations. In contrast, liquid-phase methods have emerged as a prevalent technological tool in current research. These methods offer the advantage of fine-tuning synthetic parameters across multiple scales and aspects, enabling precise catalyst design. Within the realm of liquid-phase methods, solvothermal and hydrothermal techniques stand out as two of the most commonly employed synthesis methods.

4.1. Hydrothermal Method. The hydrothermal method possesses numerous advantages, including straightforward operation, low energy consumption, and reproducibility. It effectively facilitates the preparation of nanoscale materials, enabling the synthesis of nanosized catalysts. This approach significantly overcomes the limitations associated with solid-phase methods due to their larger particle sizes, thereby offering broad application prospects in the realm of material preparation. Furthermore, in the synthesis of In-based metal sulfides, the reaction time and temperature are crucial factors. Additionally, the choice of surfactant, pH, and the type of S source play pivotal roles in the precise control of material morphology.

Jiang et al.[76] successfully synthesized nano-octahedral $CdIn_2S_4$ particles with a size approximately 70 nm using thioacetamide (TAA) as the sulfur source. The nanoparticles exhibited smooth surfaces and a relatively uniform distribution. Further, Yin et al.[77] explored the impact of various sulfur sources, namely L-cysteine, thioacetamide, and thiourea, on the synthesis of $CdIn_2S_4$. Their findings revealed that the choice of sulfur source significantly influenced the morphology, surface area, and photocatalytic activity of $CdIn_2S_4$. When L-cysteine served as the sulfur source, its robust coordination capacity facilitated the formation of a precursor complex, leading to $CdIn_2S_4$ with a larger surface area and a more symmetrical spherical morphology. This morphology enhancement contributed to the improved light-absorbing capability and an increase in active sites. In contrast, $CdIn_2S_4$ synthesized using thioacetamide and thiourea as sulfur sources exhibited a smaller surface area and higher crystallinity but displayed an irregular morphology, resulting in a decrease in photocatalytic performance. Remarkably, $CdIn_2S_4$ demonstrated the optimal reaction rate in the photocatalytic reduction of CO_2 to dimethyl methanol (2968 $\mu mol \cdot g^{-1}\ h^{-1}$) and formic acid (5258 $\mu mol \cdot g^{-1}\ h^{-1}$).

Bhirud et al.[78] conducted a thorough investigation into the influence of surfactants on the morphology and microstructure of $CdIn_2S_4$, utilizing polyvinylpyrrolidone (PVP) and cetyltrimethylammonium bromide (CTAB) as surfactants. Their findings revealed that surfactants play a pivotal role in shaping the crystal growth of $CdIn_2S_4$, leading to the production of purer and better crystalline products. Notably, $CdIn_2S_4$ synthesized with PVP assistance exhibited a highly crystalline biconical structure, which demonstrated superior photocatalytic activity compared to other samples due to its enhanced crystallinity despite having a smaller surface area. Furthermore, the study reported by Bai et al.[79] underscored the significance of surfactant concentration in determining the morphology of In-based sulfides. In the absence of cetylpyridinium bromide (CPBr), $ZnIn_2S_4$ exhibited an open and fluffy structure. However, with the introduction of CPBr, $ZnIn_2S_4$ crystallites self-organized into nanosheets and aggregated into flower-like microspheres, accompanied by the formation of slit-like pores ranging from 100 to 500 nm on the surface. This phenomenon is attributed to the orienting effect of micelles formed by CPBr molecules in solution, which directs the crystal growth and arranges the $ZnIn_2S_4$ particles in a specific manner. In addition, the concentration of CPBr also affects the morphology of microspheres, and when the amount of CPBr in the aqueous solution is 0.21 g (6.8×10^{-3} mol·L^{-1}), the formation of spherical micelles is favorable for the formation of microspheres with regular slit pores. The aggregation of microspheres became more pronounced as the amount of CPBr increased (Figure 4). In this work, the authors also investigated the role of pH in the hydrothermal process. When the pH was too low (such as 1.0), it leaded to irregular agglomerates without porous structure. As the pH rised to 1.5, a number of lamellar petals rather than microspheres were formed. When the pH was 2.0, well-structured flower-like $ZnIn_2S_4$ microspheres with tight petals and excellent porosity could be obtained, which helped the effective transfer of electron−hole pairs and thus inhibited their recombination. Second, the $ZnIn_2S_4$ samples at this time produced a quantum size effect with the largest absorption edge (530 nm, corresponding to a band gap of 2.34 eV), and the absorption edge was blueshifted toward the visible region, which enabled the material to better absorb photons and thus enhance the photocatalytic activity. However, at a pH of about 3.0, the product became a mixture of petals and microaggregates, which could be attributed to the decomposition of TAA in acidic aqueous solution and the release of H_2S, which provided S^{2-} reacting with Zn^{2+} and In^{3+} to produce a yellow precipitate. Therefore, the structural morphology of the photocatalysts can

https://doi.org/10.1021/acsomega.4c09487
ACS Omega 2025, 10, 8793−8815

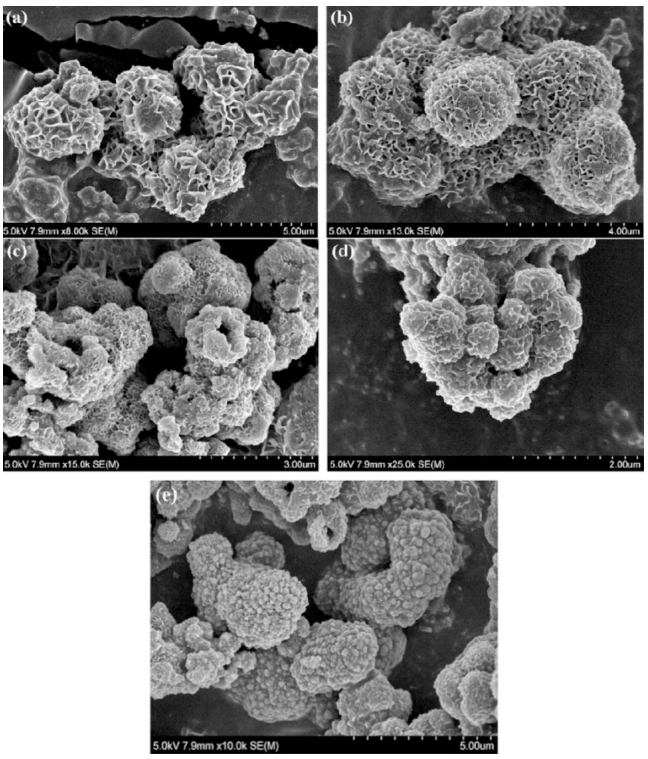

Figure 4. SEM images of $ZnIn_2S_4$ prepared with different CPBr dosages: (a) 0 g, (b) 0.21 g, (c) 0.37 g, (d) 0.67 g and (e) 1.21 g. Reprinted with permission from ref 79. Copyright 2011, Elsevier.

be optimized by tuning the reaction parameters when preparing In-based metal sulfides using hydrothermal reaction, thus achieving efficient and stable catalytic performance.

4.2. Solvothermal Method. Solvothermal process can be regarded as a development and deepening of hydrothermal process. In the solvothermal reaction, nonaqueous solvents are used as the reaction medium, and the chemical reaction of the reaction material is induced by regulating the reaction temperature and pressure. Due to the diverse and unique properties of the solvents, such as different viscosities, polarities and coordination abilities, these properties are fully demonstrated during the synthesis process to achieve precise regulation of the target products.

Differences in the solvents utilized resulted in the synthesis of materials exhibiting distinct structural characteristics. Du et al.[80] effectively tailored the preparation of $ZnIn_2S_4$ into bilayer and monolayer forms by altering the solvent. When the solvent was substituted with a 50% ethanol solution, the thickness of $ZnIn_2S_4$ was significantly reduced to 1.29 nm, equivalent to a single cell layer. This reduction in thickness facilitated efficient carrier migration to the surface, minimizing diffusion distances, thereby enhancing the separation rate and photoreduction capabilities. It is noteworthy that the synthesis of ternary metal sulfides with nanotube morphology remains a relatively uncommon and challenging task. Gou et al.[81] successfully overcame these obstacles. They controlled of the $ZnIn_2S_4$ shape by adjusting the reaction solvents (including pyridine, alcohol, acetonitrile) and temperature range (120−180 °C). By controlling reaction conditions and introducing surfactants, $ZnIn_2S_4$ nanotubes, nanoribbons, nanowires and microspheres could be selectively prepared (Table 2). These nano and microscopic structures had strong absorption over a wide wavelength range from visible to ultraviolet light, and exhibit strong excitation and emission luminescence at room temperature in the prepared microspheres. On the basis of experimental data, the related mechanisms of phase formation and morphology control of $ZnIn_2S_4$ were proposed and discussed (Figure 5). The phase formation mechanism of $ZnIn_2S_4$ involved the coordination modes of ions in solution and the retention of these coordination modes in the solid product, which determined the final crystal phase. Based on the solution coordination model (SCM), the formation of cubic and hexagonal $ZnIn_2S_4$ was explained. In terms of morphology control, the formation of $ZnIn_2S_4$ nanotubes involved a nucleation step and a self-growth step, in which the layered intermediate can be curled into a tubular structure under the right conditions. The formation of nanoribbons was the result of the growth of layered intermediates directly in the (002) direction. The $ZnIn_2S_4$ microspheres were synthesized by hydrothermal method using CTAB or PEG as structure guiding agent. The microspheres formed with the help of CTAB have stable structure, while the microspheres formed with the help of PEG can be dispersed into nanowires after ultrasonic treatment. These chemical methodologies can be utilized for the synthesis of $CuInS_2$ and $CuInSe_2$ microspheres with diverse surface morphologies, offering novel perspectives on the controlled fabrication of tailored nano- and micromaterials.

Similarly, as shown in Figure 6, Song et al.[82] synthesized $ZnIn_2S_4$ photocatalyst using water or ethylene glycol as solvent at different temperatures (120−180 °C). The synthesized samples have different spherical structures (Figure 6a−d). Specifically, EG-120, EG-150, and EG-180 exhibited a rose-like spherical structure, with EG-120 displaying larger interpetal gaps compared to DI-120 (synthesized via hydrothermal method). The expanded interlayer spacing facilitates a greater number of active sites, thereby enhancing photocatalytic activity. Moreover, the augmentation of this interlayer gap signifies an increased surface area available for the adsorption and transformation of reactants on the photocatalyst, which in

Table 2. Comparison of Synthesis Methods of $ZnIn_2S_4$ Composites with Different Morphologies

Morphology	Synthesis method	Reaction condition	Growth mechanism
$ZnIn_2S_4$ nanotubes	Solvothermal method	Pyridine as solvent; the reaction temperature was 180 °C	Self-assembly and anisotropic growth of layered intermediates
$ZnIn_2S_4$ nanoribbons	Solvothermal method	Pyridine as solvent; the reaction temperature was below 170 °C	The layered intermediates grow directly in the direction (002)
$ZnIn_2S_4$ nanowires	Hydrothermal method	PEG[a]-6000 as a surfactant; ultrasonic treatment	The layered intermediates were formed with PEG-6000
$ZnIn_2S_4$ microspheres	Hydrothermal method	CTAB[b] as a surfactant	Surfactant template technology

[a]PEG: Polyethylene glycol. [b]CTAB: Hexadecyl trimethylammonium bromide.

https://doi.org/10.1021/acsomega.4c09487
ACS Omega 2025, 10, 8793−8815

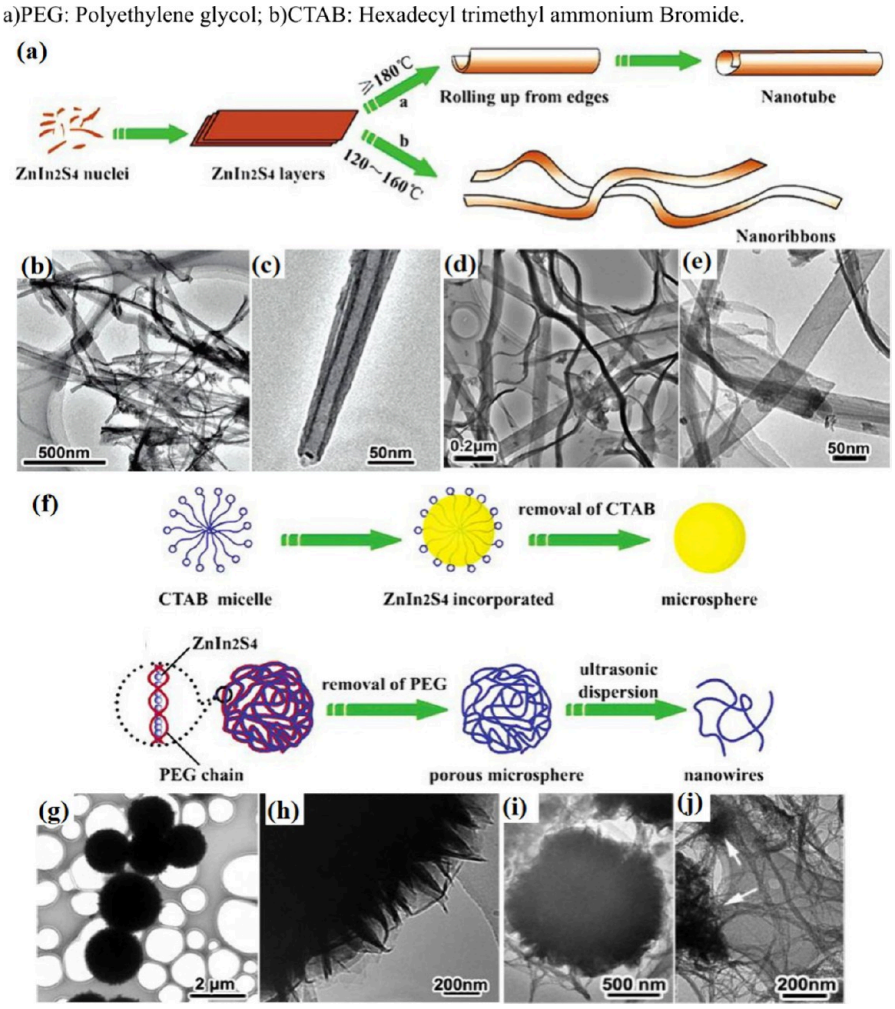

Figure 5. (a) Schematic diagram of the growth mechanism of $ZnIn_2S_4$ nanotubes and nanoribbons, TEM images of (b, c) $ZnIn_2S_4$ nanotubes synthesized by solvothermal method at 180 °C, (d, e) $ZnIn_2S_4$ nanoribbons synthesized by solvothermal method at 160 °C, (f) schematic diagram of the growth mechanism of $ZnIn_2S_4$ microspheres and nanowires in the presence of CTAB and PEG-6000, (g, h) CTAB and (i, j) PEG-6000 assisted $ZnIn_2S_4$ microspheres/nanowires synthesized by hydrothermal method. Reprinted with permission from ref 81. Copyright 2006, Elsevier.

turn optimizes the photocatalytic efficiency. Consequently, $ZnIn_2S_4$ synthesized in ethylene glycol at 120 °C (EG-120) exhibits outstanding photocatalytic performance. Furthermore, EG-120 exhibited superior separation of photogenerated carriers and exceptional stability, as evidenced by photoluminescence and transient photocurrent response analyses.

4.3. Spray Pyrolysis Method. Spray pyrolysis technology has been widely used in the preparation of semiconductor films, superconductor powders, multicomponent ceramics, catalysts and electrode materials. Compared with traditional methods such as hydrothermal synthesis, this technology has significant advantages in adjusting material properties, enabling online adjustments such as stoichiometric ratio, phase composition, particle size, specific surface area, etc. In addition, spray pyrolysis technology is excellent in the preparation of uniform composite materials, multicomponent materials with accurate stoichiometric ratios, pore structures and hollow structures, and has the convenience of large-scale production. Compared with powders prepared by other methods, powders prepared by spray pyrolysis usually have higher crystallinity, less caking, and higher purity.[83,84]

In related studies, silver-doped indium sulfide films were successfully prepared by spray pyrolysis technology.[85] The obtained samples were then annealed in air and vacuum at 400 °C for 2 h. It was found that the prepared films were polycrystalline and showed the tetragonal β phase structure of In_2S_3. The grain size of vacuum annealed and air annealed samples increased by 27% and 74%, and the roughness of the films increased by 20% and 56%, respectively, but the optical transmittance decreased significantly. Under vacuum annealing and air annealing conditions, the optical band gap of the film decreases from 2.71 to 2.45 and 2.39 eV respectively. Li et al.[86] prepared $ZnIn_2S_4$ film on doped indium tin oxide (ITO) glass substrate by using a mixed aqueous solution of $ZnCl_2$, $InCl_3$ and $(NH_2)_2CS$ through an economical and efficient spray pyrolysis technology. The obtained grain size is about 120−200 nm and has a cubic spinel structure. The optical band gap of the film is about 2.1 eV, showing good photoelectrochemical properties and relative stability in the visible region. The Enesca research team[87] prepared photoactive heterostructures based on SnO_2, TiO_2 and $CuInS_2$ by robotic spray pyrolysis. The samples containing metal oxides appear granular with an average roughness of 30 nm, while the samples containing $CuInS_2$ appear multishaped aggregates with an average roughness of 50 nm with good UV and visible light absorption properties, which increases the number of photons that may be

https://doi.org/10.1021/acsomega.4c09487
ACS Omega 2025, 10, 8793−8815

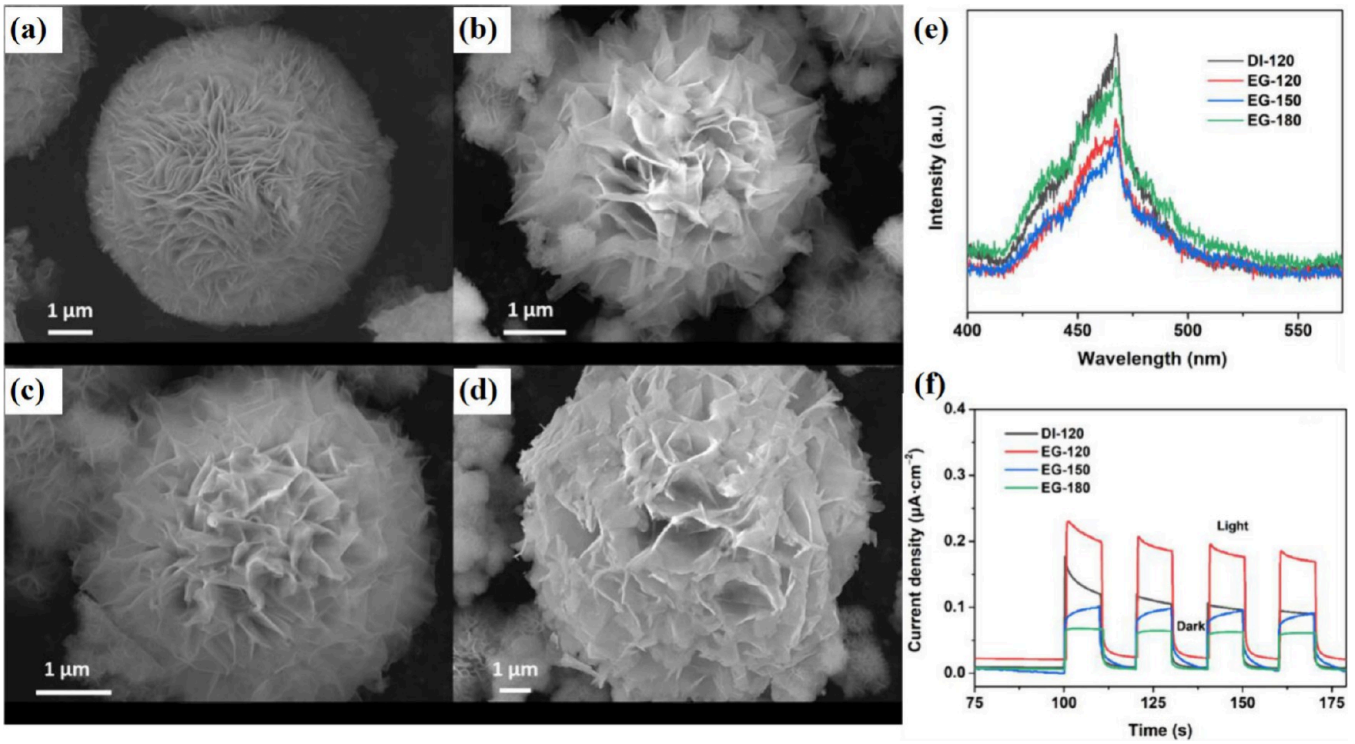

Figure 6. SEM of (a) DI-120, (b) EG-120, (c) EG-150 and (d) EG-180, (e) photoluminescence spectra, and (f) transient photocurrent response of different $ZnIn_2S_4$ photocatalysts. Reprinted with permission from ref 82.

converted during photocatalysis. Energy level estimation shows that the CIS_TiO_2_SnO_2 sample has a suitable band structure, which is conducive to the generation and migration of charge carriers, and thus shows a high photocatalytic efficiency. Despite its advantages, spray pyrolysis has some limitations, including low yield, drying and calcination steps, and impurities in the solvent may contaminate the final product.

4.4. Other Methods. In addition to the above introduction, the preparation strategies also include sol−gel method,[88,89] calcination method,[90] electrodeposition method,[91] coprecipitation method,[92] microwave-assisted method,[93] etc. With the continuous progress of materials science, new synthesis technologies emerge in endlessly, aiming to improve the performance and application fields of indium-based sulfide. For example, the self-template strategy[94] involves two ion exchange reactions. In the initial stage, In_2S_3 nanotubes were prepared by liquid phase vulcanization using in based metal organic framework (MIL-68) hexagonal prism as precursor. Subsequently, the as prepared In_2S_3 tubular nanostructures were transformed into In_2S_3-$CdIn_2S_4$ hybrid nanotubes by effective cation exchange reaction. By adjusting the reaction time, the composition of the final composite can be accurately controlled, so that two different sulfide semiconductors can be effectively integrated into a hierarchical tubular hybrid with uniform interface contact and ultrathin two-dimensional (2D) nanosheet subunits. Layered heterostructure nanotubes significantly promote the separation and migration of photoinduced carriers, enhance the adsorption capacity and concentration of CO_2 molecules, and provide rich active sites for surface redox reactions. Thanks to these unique structure and composition characteristics, the optimized hierarchical In_2S_3-$CdIn_2S_4$ nanotubes do not need any noble metal cocatalysts in the catalytic system, showing excellent co generation rate (825 μmol·h^{-1} g^{-1}) and stability under visible light. Each preparation method has its specific advantages and limitations. The selection of appropriate preparation methods depends on the application requirements and performance indicators of materials. The continuous development of materials science and the emergence of new synthetic technologies provide more possibilities for improving the properties and application fields of indium-based sulfides.

5. MODIFICATION STRATEGIES FOR In-BASED METAL SULFIDES

Although numerous photocatalysts have been reported and efforts have been made to apply them in real-world scenarios as soon as possible, problems such as low efficiency, insufficient selectivity, and poor stability still severely limit the progress in this field. Therefore, there is a need not only to continue to develop new and efficient catalysts, but also to modify conventional catalysts to enhance their performance. Photocatalysis is a highly intricate process encompassing numerous intricate steps, encompassing light harvesting, charge segregation and transportation, as well as redox reactions occurring on the surface. Ideal photocatalysts ought to strike a balance between thermodynamic and kinetic considerations. Specifically, they should exhibit a broad light absorption spectrum, efficient electron−hole separation and transport capabilities, and accelerated kinetics for surface reactions. In order to improve the photocatalytic efficiency, the structure of the photocatalyst needs to be carefully designed to reduce the recombination of photogenerated carriers. Currently, many modification strategies have been developed to improve the photocatalytic activity and selectivity of CO_2 reduction on metal sulfides in an effective and feasible way, including heterostructure construction, element doping, defect engineering, co-catalyst loading, etc. Table 3 summarizes In-based

https://doi.org/10.1021/acsomega.4c09487
ACS Omega 2025, 10, 8793−8815

Table 3. Evaluation of Photocatalytic CO_2 Reduction Performance of Different Catalytic Systems

Photocatalyst	Synthetic method	Reductant	Light source	Product	Yield ($\mu mol \cdot g^{-1}\ h^{-1}$)	Ref.
$ZnIn_2S_4/g\text{-}C_3N_4$	Solvothermal method	H_2O, TEOA, MeCN[a]	300 W Xe lamp	CO	883	39
$ZnIn_2S_4$/Au/CdS	Photodeposition	H_2O, TEOA	300 W Xe lamp	CO	63.07	43
In_2S_3/NiAl-LDH	Hydrothermal approach	H_2O	300 W Xe lamp	CH_4	36.1	48
In_2S_3/WS_2	Hydrothermal method	H_2O, TEOA	300 W Xe lamp	CO	17.8	49
				CH_4	15.7	
In_2O_3/In_2S_3	Hydrothermal method	H_2O	300 W Xe lamp	CO	2.59	50
				CH_4	14.3	
Hexagonal $ZnIn_2S_4$	Lamellar hybrid	CH_3OH	250 W high-pressure mercury lamp	MF[b]	190.59	52
$ZnIn_2S_4\text{-}In_2O_3$	Hydrothermal method	Bpy,[c] $CoCl_2$, TEOA, H_2O, MECN	300 W Xe lamp	CO	3075	53
$ZnIn_2S_4$/N-graphene	Hydrothermal method	H_2O, Na_2SO_3	300 W Xe lamp	CH_4	1.01	54
				CO	2.45	
				CH_3OH	1.37	
Ce/Zr-UiO-66-NH_2/$CdIn_2S_4$	Hydrothermal method	H_2O	Simulated solar irradiation	CO	6.01	56
$AgInS_2$@PEI QDs	Hydrothermal method	MECN, H_2O, TEOA	300 W Xe lamp	C_2H_6	10.5	59
G-C_3N_4@Cu-In-Zn-S	Electrostatic self-assembly	H_2O	300 W Xe lamp	CO	3.73	65
				CH_4	2.36	
Vs-In_2S_3/$CuInS_2$	Solvothermal method	H_2O, Na_2SO_3	300 W Xe lamp	CO	80.3	74
				CH_4	11.8	
$WO_3/ZnIn_2S_4$	Precipitation method	H_2O	300 W Xe lamp	CO	51.3	75
				CH_4	58.7	
$Znln_2S_4$/biochar	Precipitation method	H_2O, TEOA	300 W Xe lamp	CO	20.7	90
In_2S_3-$CdIn_2S_4$	Sequential anion- and cation-exchange reactions	Bpy, $CoCl_2$, TEOA, H_2O, MECN	300 W Xe lamp	CO	825	94
Co_3O_4@$CdIn_2S_4$	Solvothermal method	Bpy, $CoCl_2$, TEOA, H_2O, MECN	300 W Xe lamp	CO	5300	96
MnS/In_2S_3	Solvothermal method	MECN, TEOA	300 W Xe lamp	CO	58	97
$CuInS_2$@TCOF[d]	Solvothermal method	CH_3CN, TEOA	300 W Xe lamp	HCOOH	171.2	98
In_2S_3/MnO_2/BiOCl	Hydrothermal and solution combustion methods	H_2O	300 W Xe lamp	CO	63.2	100
				CH_4	42.4	
				C_2H_4	51.2	
Bi-BiOCl/$MgIn_2S_4$	$NaBH_4$ reduction and hydrothermal method	H_2O	Solar simulator	CH_4	4.29	102
$Ta_2O_5/ZnIn_2S_4$	Solvothermal method	H_2O	300 W Xe lamp	CO	101.62	103
				CH_4	7.22	
MoO_{3-x}@$ZnIn_2S_4$	Solvothermal method	H_2O	300 W Xe lamp	CO	4.65	104
				CH_4	28.3	
Er-$ZnIn_2S_4$	Hydrothermal method	TEOA	300 W Xe lamp ($\lambda \geq 420$ nm)	CO	1.56	105
				CH_4	0.026	
Sn-$MgIn_2S_4$	Hydrothermal method	H_2O, TEOA	300 W Xe lamp	CO	0.425	106
				CH_4	0.0325	
P-$ZnIn_2S_4$	Hydrothermal method	$CoCl_2$, Bpy, MECN, H_2O, TEOA	300 W Xe lamp ($\lambda \geq 420$ nm)	CO	476	107
C-In_2S_3	Hydrothermal method	H_2O	300 W Xe lamp	C_2H_4	26.6 ± 4.1	108
Ultrathin-g-C_3N_4@$ZnIn_2S_4$/SWNTs	Hydrothermal method	NaOH, TEOA	300 W Xe lamp	CO	33.7	114
				CH_4	39.8	
$CuInS_2/C/TiO_2$	Hydrothermal method	H_2O	300 W Xe lamp ($\lambda > 420$ nm)	CO	7.73	116
CuAu-$SnIn_4S_8$	Hydrothermal method and reduction	TEOA, H_2O	300 W Xe lamp	CO	27.87	117
				CH_4	7.21	

[a]MeCN: acetonitrile. [b]MF: methyl formate. [c]Bpy: 2′2-bipyridine. [d]TCOF: a triazine-based COF with an electron-rich and large π-conjugated system.

sulfide photocatalysts with various modification strategies and their CO_2 photoreduction activities.

5.1. Construct Heterojunctions. During the photocatalytic reduction of CO_2, the recombination of photogenerated carriers presents a pivotal challenge that requires resolution. To surmount this obstacle, the creation of heterostructures is particularly vital. By combining semiconductor materials with different band structures, hetero-

https://doi.org/10.1021/acsomega.4c09487
ACS Omega 2025, 10, 8793−8815

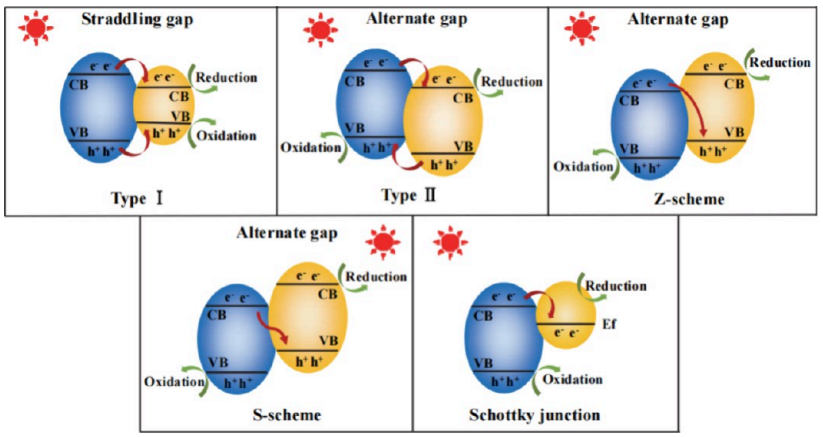

Figure 7. Heterojunctions of type-I heterojunctions, type II heterojunctions, Z-scheme heterojunctions, S-scheme heterojunctions and Schottky junctions. Reprinted with permission from ref 95. Copyright 2023, Elsevier.

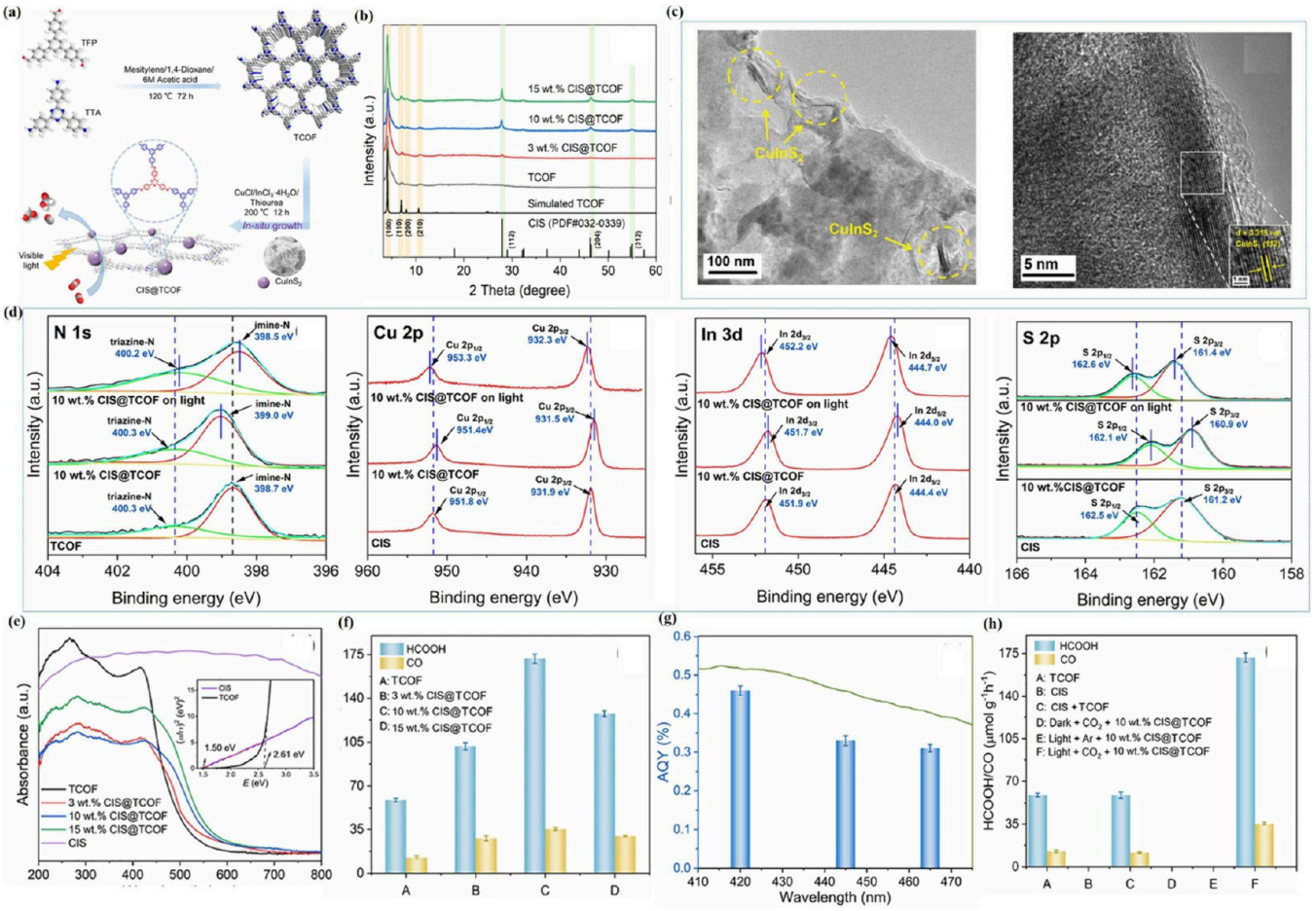

Figure 8. (a) Schematic diagram of the synthesis of CIS@TCOF heterostructure, (b) XRD patterns, (c) TEM images of 10 wt % CIS@TCOF, (d) XPS spectra of the as-synthesized samples, (e) UV−vis DRS of the synthesized sample, (f) amount of HCOOH and CO produced by the photocatalysts under visible light irradiation, (g) AQY calculated for the photocatalytic reduction of CO_2 by 10 wt % CIS@TCOF, (h) comparison of photocatalytic activity of different photocatalysts or under different conditions. Reprinted with permission from ref 98.

structures notably broaden the visible light absorption spectrum of the photocatalysts, thereby markedly enhancing photocatalytic efficiency. This structural design not only helps to form a built-in electric field between different materials, effectively promoting the separation of photogenerated electrons and holes and reducing their complexation rate, but also prolongs the lifetime of the photogenerated electron−hole pairs and enhances the reduction ability of the semiconductor through careful regulation, which significantly improves the photoquantum efficiency. Moreover, the heterostructures can direct specific photocatalytic reaction pathways and optimize the selectivity of target products, further elevating the efficiency and controllability of the photocatalytic process..Presently, the prevalent types of

https://doi.org/10.1021/acsomega.4c09487
ACS Omega 2025, 10, 8793−8815

heterojunctions encompass various configurations such as Type-I, Type-II, Z-scheme, S-scheme, and Schottky structure (Figure 7).[95] To establish effective heterojunctions, it is imperative to ensure that the chosen materials exhibit a high degree of compatibility in terms of energy band structure and crystal structure, which is crucial for achieving efficient photocatalytic performance.

A p−n heterojunction is a typical representative of type-II heterostructures. When a p-type semiconductor and an n-type semiconductor are in contact with each other, they naturally form a p−n heterojunction at the interface due to the diffusion effect of electrons and holes. This structure not only establishes a space charge region, but also generates a strong built-in electric field that effectively guides electrons and holes in opposite directions. Under light irradiation, the photogenerated electrons and holes can be rapidly separated with the help of this strong built-in electric field and are rapidly transferred to different ends of the heterojunction.[96] The mechanism of spatial carrier separation proves advantageous in enhancing the redox capabilities of the catalyst.

For instance, MnS acts as a p-type semiconductor characterized by a band gap of 2.68 eV, a conduction band minimum (CBM) located at approximately 1.52 V, and a valence band maximum (VBM) situated at around 2.68 eV.[97] Conversely, In_2S_3 is classified as an n-type semiconductor with a band gap of 2.15 eV, a CBM at roughly −0.42 V, and a VBM at approximately 2.15 eV. The incorporation of Mn^{2+} ions into MIL-68(In) submicron rods, followed by a vulcanization process, leads to the creation of a tubular structure composed of MnS and In_2S_3 nanosheets. This structure simultaneously forms numerous MnS/In_2S_3 p−n heterostructures. Under light irradiation, the p−n junction of the MnS/In_2S_3 heterostructure generates a robust internal electric field. This field facilitates the separation and migration of photogenerated electrons and holes. Electrons generated by light tend to move from MnS's CB to that of In_2S_3, whereas holes traverse from In_2S_3's VB to MnS's valence band. This mechanism of charge separation and migration notably enhances the photocatalytic efficiency of the catalyst in reducing CO_2. Compared to the pristine MnS and In_2S_3, the prepared MnS/In_2S_3 heterojunctions showed excellent performance by increasing the photocatalytic activity for CO_2 reduction by up to four times. The optimal CO product rate was 58 $\mu mol \cdot g^{-1}\ h^{-1}$ in the MnS/In_2S_3 (30 wt %). Chang et al.[98] explored the band structure and photochemical mechanism of a photocatalyst via a range of experiments and theoretical computations. Utilizing a triazine-based covalent organic framework (TCOF) and $CuInS_2$ (CIS), they engineered a p−n heterostructure that yielded an effective, precious metal-free photocatalyst for CO_2 reduction (Figure 8). In the CIS@TCOF complex, the binding energies of Cu 2p, In 3d and S 2p shift negatively with respect to pure CIS and TCOF, while the binding energies of N 1s shift positively. This change accords with the general rule of heterojunction type photocatalyst, indicating that p−n heterojunction was formed when CIS and TCOF contact. TCOF, an n-type semiconductor, possesses a CB potential proximate to its flat-band potential, estimated at −0.95 V vs NHE. Conversely, CIS, a p-type semiconductor, has a VB potential estimated at 1.07 V vs NHE. The band gap energies of TCOF and CIS were calculated to be 2.61 and 1.50 eV, respectively. Upon contact, the formation of p−n heterojunctions between TCOF and CIS led to the emergence of a built-in electric field at the junction interface. This internal electric field facilitated the migration of photogenerated carriers, suppressed the recombination of electron−hole pairs, and enhanced the photocatalytic efficiency. During the photocatalytic process, electrons transferred from the CIS's CB to the TCOF's CB to engage in CO_2 reduction, whereas holes moved from the TCOF's VB to the CIS's VB, where they were consumed by sacrificial agents. Furthermore, the work functions (Φ) of TCOF and CIS were ascertained through DFT calculations, measuring 4.59 and 5.45 eV, respectively. The computational outcomes indicated that contact between TCOF and CIS induced Fermi energy level (E_F) equilibrium, resulting in the creation of an internal electric field that further enhanced the transfer of photogenerated carriers. Compared with TCOF, the photocatalytic performance of CIS@TCOF heterostructure was significantly improved. Under visible light irradiation, the yield of HCOOH reached 171.2 $\mu mol \cdot g^{-1}\ h^{-1}$, which was about 3 times that of TCOF. The photocatalytic CO_2 reduction activity of 10 wt % CIS@TCOF did not change significantly after repeated use for five times. In addition, the calculated results for 10 wt % CIS@TCOF AQYs at wavelengths of 420, 445, and 465 nm were 0.46%, 0.33%, and 0.31%, respectively. The photocatalyst exhibits good photocatalytic performance in the visible light region, particularly at a wavelength of 420 nm.

Z-scheme heterojunctions, also known as space-separated heterojunctions, are distinctly different from conventional p−n heterojunctions in the photocatalytic process. In p−n heterojunctions, electron−hole pairs generated by photoexcitation are directly recombined at the contact interface, whereas in Z-scheme structures, electrons and holes are spatially separated and migrate in two different semiconductor materials, avoiding the compounding of charges during the transport process while maintaining the reduction and oxidation capabilities of the carriers. Consider, for instance, the Sn-In_2O_3/In_2S_3 photocatalysts, where Sn-In_2O_3 functions as an n-type semiconductor and In_2S_3 as a p-type semiconductor. The band structures of In_2O_3 and In_2S_3 are effectively integrated through a direct Z-scheme heterojunction.[99] The CB of In_2O_3 is positioned lower than the reduction potential of protons or CO_2, whereas the VB of In_2S_3 is more apt for the oxidation of OH^- or H_2O to generate ·OH radicals. This configuration encourages photogenerated holes to remain within the VB of In_2O_3, while photogenerated electrons are inclined to migrate from the CB of In_2O_3 to the VB of In_2S_3, establishing direct Z-scheme heterojunctions. This not only widens the spectrum of light absorption but also enhances charge separation and transfer kinetics, thereby accelerating the photocatalytic reaction. Furthermore, due to favorable lattice compatibility, heterojunctions exhibit fewer defect traps, significantly reducing the recombination of photogenerated carriers and thus enhancing the redox capacity of the carriers released into the photocatalyst. When Sn-In_2O_3/In_2S_3 was employed as a photocatalyst, the CH_4 yield attained 0.41 $\mu mol \cdot cm^{-2}\ h^{-1}$ and the CO yield reached 1.03 $\mu mol \cdot cm^{-2}\ h^{-1}$. In a separate report, Chen et al.[100] effectively cultivated BiOCl nanosheets on In_2S_3 nanoflowers situated on the MnO_2 nanowires' surface using a two-step hydrothermal technique, subsequently synthesizing In_2S_3/MnO_2/BiOCl double Z-scheme heterostructures. This setup facilitates electron transfer from the MnO_2 CB to the In_2S_3 VB, while electrons are shuttled from the In_2S_3 CB to the BiOCl VB. An electron depletion and accumulation layer forms near the MnO_2/In_2S_3 and In_2S_3/BiOCl interfaces, resulting in an internal electric field from MnO_2 to BiOCl that expedites the transfer of

https://doi.org/10.1021/acsomega.4c09487
ACS Omega 2025, 10, 8793−8815

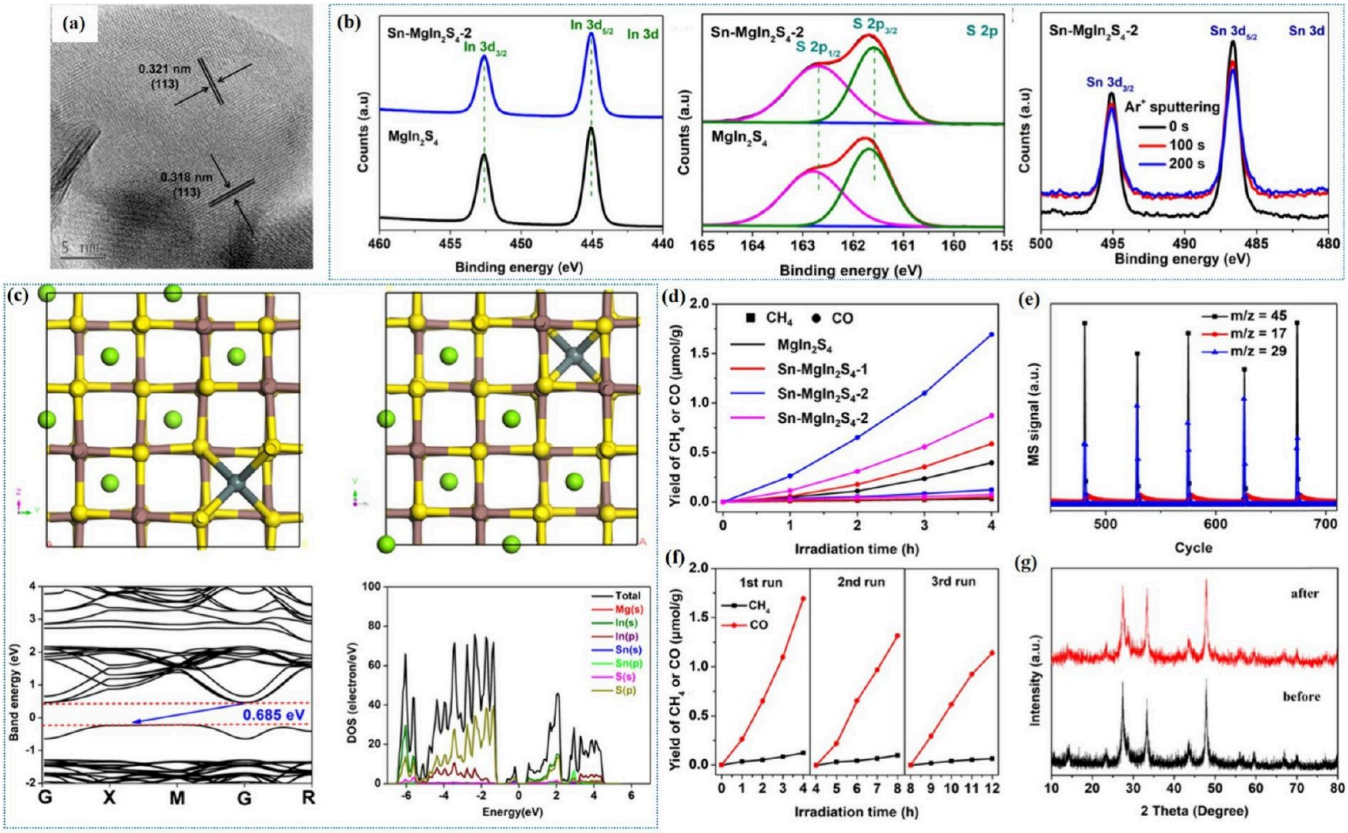

Figure 9. (a) TEM image of Sn-$MgIn_2S_4$-2, (b) high-resolution XPS spectra of In and S for $MgIn_2S_4$ and Sn-$MgIn_2S_4$-2, time-dependent high-resolution Sn 3d XPS spectra upon Ar^+ sputtering for Sn-$MgIn_2S_4$-2, (c) side and top views of the Sn-$MgIn_2S_4$ model structure, simulated electronic energy band structure and density of states (where green, brown, yellow and gray spheres represent Mg, In, S and Sn atoms, respectively), (d) CH_4 and CO yields of $MgIn_2S_4$ and Sn-$MgIn_2S_4$ photoreduction of CO_2, (e) CO_2 reduction mass spectra of Sn-$MgIn_2S_4$-2 photocatalyst in $^{13}CO_2$ atmosphere, (f) CO_2 reduction cycle suns of Sn-$MgIn_2S_4$-2 sample, (g) XRD spectra of Sn-$MgIn_2S_4$-2 sample before and after photocatalytic reaction. Reprinted with permission from ref 106. Copyright 2021, Elsevier.

photogenerated electrons, thereby enhancing the efficiency and product selectivity of photocatalytic CO_2 reduction. Notably, the Mn atoms' role within the Z-scheme heterojunction bolsters the formation selectivity of C_2H_4, rendering In_2S_3/MnO_2/BiOCl composites highly selective for C_2H_4 during the photocatalytic CO_2 reduction process. In the photoreaction, the CO yield was 51.2 μmol·g^{-1} h^{-1}, CH_4 yield was 42.4 μmol·g^{-1} h^{-1}, and C_2H_4 yield was 63.2 μmol·g^{-1} h^{-1}, which were 3.94-fold, 5.5-fold, and 3.64-fold greater than that of pure In_2S_3, respectively.

In recent years, S-scheme heterojunctions have become one of the highly sought-after heterostructures due to their excellent light trapping ability, strong redox potentials, efficient charge separation rates, and superior stability.[101] Zhang et al.[102] successfully prepared Bi-BiOCl/$MgIn_2S_4$ heterostructures (BBOC/MIS) by $NaBH_4$ reduction and in situ hydrothermal process and its application to photocatalytic CO_2 reduction. A portion of ultrasonically exfoliated BBOC ultrathin nanosheets was grown on the surface of MIS microspheres, and another portion of BBOC and MIS served as the core and shell of BBOC/MIS, respectively. The morphology, energy band arrangement, optical and electronic properties of the photocatalysts were tested by various characterization methods.The BBOC/MIS heterojunction has excellent photocatalytic performance and excellent reusability, and is capable of reducing CO_2 to CH_4 under simulated sunlight irradiation in water without any sacrificial agent.The experimental results show that 6% of the BBOC/MIS samples exhibit the best performance in photocatalytic reduction of CO_2 exhibits the best photocatalytic performance with a maximum CH_4 yield of up to 4.29 μmol·g^{-1} h^{-1}, which is about 7.56 times higher than that of the pure MIS.The enhanced photocatalytic performance of BBOC/MIS is mainly attributed to its improved visible-light responsiveness as well as its efficient photogenerated electron−hole pair separation through the S-scheme heterojunction interface. In addition, the metal Bi, as a bridge connecting BOC and MIS, played a key role in promoting charge transfer, which greatly facilitated the photocatalytic reduction of CO_2 to CH_4. Wang et al.[103] prepared core−shell-structured Ta_2O_5/$ZnIn_2S_4$ nanofibers by in situ growth technique. The prepared Ta_2O_5/$ZnIn_2S_4$ S-scheme heterojunction has significantly enhanced CO_2 reduction activity, and the total CO_2 conversion (including CO and CH_4) on $ZISTO_{0.1}$ is 4.1 and 5.74 times higher than that of the pristine Ta_2O_5 nanofibers and $ZnIn_2S_4$ nanosheets, respectively. Lei et al.[104] successfully designed an oxygen vacancy-modified MO_{3-x}@$ZnIn_2S_4$ photocatalyst by in situ growth of $ZnIn_2S_4$ on the rod-like MoO_{3-x} surface. This composite photocatalyst exhibited excellent performance under UV−vis-IR radiation by virtue of its unique hierarchical structure, tight interfacial contact, special charge transfer pathway and excellent photothermal efficiency, among other synergistic effects. Without adding any sacrificial agent and co-catalyst, the average CO and CH_4 yields of this catalyst were as

https://doi.org/10.1021/acsomega.4c09487
ACS Omega 2025, 10, 8793−8815

high as 4.65 and 28.3 μmol·g^{-1} h^{-1}, respectively, a value that was enhanced by a factor of 19.4 and 11.7 compared with those of the pure MoO_{3-x} and $ZnIn_2S_4$ samples, respectively. Especially noteworthy is that the selectivity of CH_4 is even as high as 85.89%, which fully demonstrates the great potential of this photocatalyst in the fields of energy conversion and environmental protection.

5.2. Elemental Doping. The optical behavior of photoactive substances is predominantly dictated by their intrinsic electronic architecture. Nevertheless, the efficiency of their photocatalytic activity can be markedly improved by altering their chemical makeup via the incorporation of diverse elements, a process known as doping. This technique encompasses the introduction of both metallic elements, such as Zn and Cu, and nonmetallic elements, including S, B, C, N, P, and others. Elemental doping has emerged as a potent approach for the modification of semiconductors, enabling meticulous adjustment of the energy level configuration and, consequently, the modification of the material's electronic properties. Presently, metal sulfides based on In, doped with various elements, have attracted considerable interest within the scientific community. Instances of such doped materials include C-doped In_2S_4, Cu-doped $CdIn_2S_4$, and Mn-doped $ZnIn_2S_4$. These materials, modified through doping, showcase exceptional characteristics that present fresh avenues for the progression of photocatalytic technology.

The influence of element doping on photocatalyst is mainly reflected in the change of electronic structure. For example, Er doping introduced a new energy level in $ZnIn_2S_4$, which effectively narrowed the band gap and thereby substantially enhanced light absorption efficiency.[105] Furthermore, Er doping modified the electronic structure of $ZnIn_2S_4$, thus affecting the reaction pathway for CO_2 reduction. For undoped $ZnIn_2S_4$, the CO_2 reduction pathway to CH_4 with the lowest energy barrier is $CO_2 \rightarrow *COOH \rightarrow *CO \rightarrow *CHO \rightarrow *CH_2O \rightarrow *CH \rightarrow *CH_2 \rightarrow CH_3 \rightarrow CH_4$. However, in the case of Er-doped $ZnIn_2S_4$, the generation of OCH_3 surface species occurred due to the reduced bond energy of the coordination bond between O and Er. The specific reduction pathway for this material is $CO_2 \rightarrow *COOH \rightarrow *CO \rightarrow *CHO \rightarrow *OCH_2 \rightarrow *OCH_3 \rightarrow CH_4$. Er-$ZnIn_2S_4$ not only significantly lowered the reaction barrier compared to pure $ZnIn_2S_4$ but also enhanced the adsorption of key intermediates *CHO and $*CH_2O$. This augmentation aids in enhancing the selectivity of CO_2 reduction and facilitates the production of CH_4. Compared with the original $ZnIn_2S_4$, Er doped $ZnIn_2S_4$ exhibited markedly enhanced photocatalytic activity. The conversion efficiency of CO_2 to CH_4 was elevated by 256-fold, achieving over 90% selectivity.

Experimental characterization, such as TEM and XPS, and simulation analysis methods can be used to verify the introduction of ions into the photocatalyst lattice. For Sn-doped $MgIn_2S_4$, the peak displacement of Sn 3d indicates that Sn replaced the position of Mg atoms in high-resolution XPS spectra (Figure 9).[106] If Sn was present in a interstitial configuration, the electron density of the In and S atoms would change, resulting in a change in the binding energy of the In element. However, no change in the binding energy of the In element was observed, suggesting that Sn^{2+} ions were successfully introduced into the lattice of $MgIn_2S_4$, rather than being adsorbed on the surface or forming surface gradient diffusion doping. In the Ar^+ sputtering experiment, the peak intensity of Sn 3d remained constant with the extension of sputtering time, which indicates that Sn^{2+} ions were introduced into the unit cell of $MgIn_2S_4$, rather than only adsorbed on the surface. HRTEM image showed clear lattice fringes, which further confirmed the doping of Sn into the lattice of $MgIn_2S_4$. The impact of Sn ion incorporation on the electronic configuration and optical characteristics of the $MgIn_2S_4$ semiconductor was explored using density functional theory (DFT) computations. Observing from both the lateral and overhead perspectives, it becomed evident that the Sn-$MgIn_2S_4$ structure was comprised of Mg, In, S, and Sn atoms, with the Sn atom substituting for Mg. The electronic band structure diagram indicated that Sn-$MgIn_2S_4$ possessed a narrower band gap compared to $MgIn_2S_4$, transitioning from a direct to an indirect band gap. The state density diagram revealed that the conduction and valence bands of Sn-$MgIn_2S_4$ were predominantly composed of In(s)+S(p) and Sn(s)+S(p). These findings suggested that Sn doping couldn adeptly modify the band structure of $MgIn_2S_4$, converting it from a direct to an indirect band gap, and decreasing the band gap width, thereby extending the optical absorption spectrum. Specifically, Sn-$MgIn_2S_4$ had a band gap width of 0.69 eV, compared to the 1.74 eV of pure $MgIn_2S_4$. Furthermore, Sn doping enhanced the dispersion of the VBM and CBM, suggesting that Sn doping facilitates charge carrier mobility. Calculations of the effective mass revealed that the hole effective mass of Sn-$MgIn_2S_4$ was notably diminished, which further enhanced the migration of photoinduced carriers. These theoretical outcomes aligned with the heightened activity observed in Sn-doped $MgIn_2S_4$ samples during photocatalytic CO_2 reduction. Following a 4-h exposure to light, the CO and CH_4 production rates of Sn-$MgIn_2S_4$-2 were found to be 3.35 and 3.33 times greater than those of pristine $MgIn_2S_4$, respectively. Furthermore, the Sn-$MgIn_2S_4$-2 photocatalyst demonstrated photocatalytic stability, retaining over 60% of its activity after three consecutive cycles.

In view of the environmental benefits and safety characteristics, nonmetal ion-doped photocatalysts are also widely used. Qin and colleagues[107] investigated the impact of incorporating nonmetallic phosphorus (P) into the structure of $ZnIn_2S_4$ nanosheets on their photocatalytic efficiency. The synthesis of P-doped ZIS (PZIS) nanosheets was achieved through a straightforward hydrothermal process, with the precise tuning of phosphorus content facilitated by varying the concentration of NaH_2PO_4. It was shown that the doped P entered into the lattice of $ZnIn_2S_4$, reduced the crystallinity, changed the original crystal structure and local elemental coordination, and adjusted the energy band edges of $ZnIn_2S_4$. The introduced P can also be used as an additional active site for the catalytic reaction, which reduces the complexation rate of photogenerated electrons and holes and thus improves the catalytic reaction efficiency. The optimized PZIS showed a CO yield of 18.8 μmol/30 min under visible light, which was 2.5 times higher than that of pure ZIS. Wang et al.[108] conducted an in-depth study on the performance of C-doped In_2S_3 nanosheets (C-In_2S_3) as photocatalysts in converting CO_2 to C_2H_4. The experimental results showed that C-In_2S_3 exhibited high catalytic ability to effectively promote the conversion of CO_2 and H_2O to C_2H_4 at 150 °C. Specifically, the selectivity of C_2H_4 reached about 50%, while the yield was 26.6 ± 4.1 μmol·g^{-1} h^{-1}. While, the quantum efficiency at 420 nm was as high as 13.3%. In contrast, C_2H_4 production could not be detected in undoped In_2S_3 under the same conditions. In addition, the effectiveness of C-In_2S_3 nanosheets in photocatalytic CO_2

https://doi.org/10.1021/acsomega.4c09487
ACS Omega 2025, 10, 8793−8815

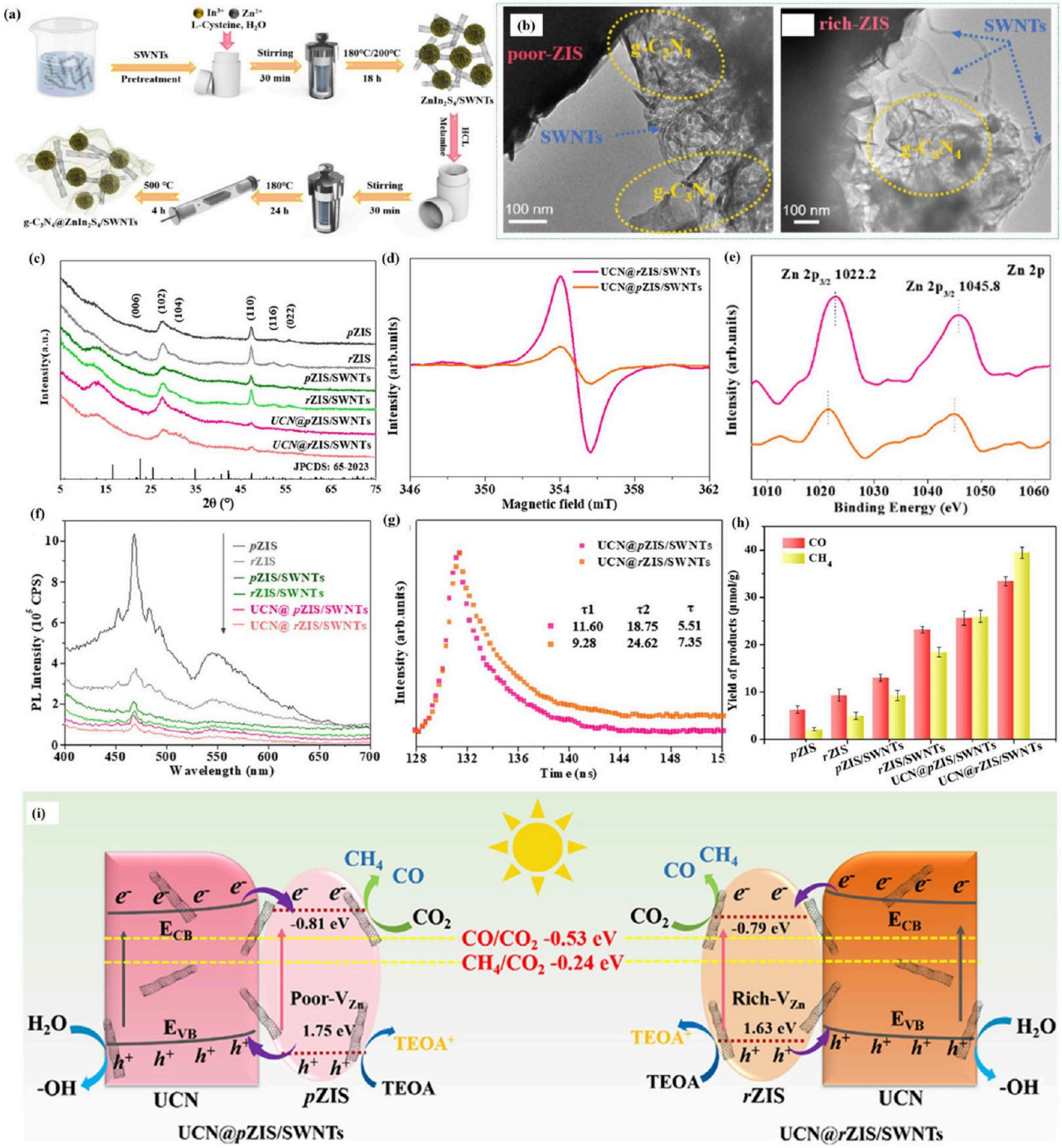

Figure 10. (a) The synthesis route of UCN@ZIS/SWNTs photocatalyst, (b) TEM images of as-prepared UCN@pZIS/SWNTs and UCN@rZIS/SWNTs composite, (c) XRD of as-prepared samples, (d) EPR spectra and (e) XPS high-resolution spectrum of Zn 2p of UCN@pZIS/SWNTs and UCN@rZIS/SWNTs, (f) PL spectra and (g) time-resolved PL decay curves for samples, (h) performance of photoreduction of CO_2 into CH_4 or CO, (i) electron transfer pathways for photoreduction of CO_2 by UCN@pZIS/SWNTs and UCN@rZIS/SWNTs composites. Reprinted with permission from ref 114. Copyright 2023, Elsevier.

reduction was further verified by performing $^{13}CO_2$ and D_2O isotope labeling experiments, which confirmed that both carbon and hydrogen sources in C_2H_4 were derived from CO_2 and H_2O. It was also found that C doping not only accelerated the adsorption and activation process of CO_2, but also significantly lowered the energy barrier required for the formation of the key intermediate CH*, thus significantly improving the selectivity of C_2H_4. It is worth mentioning that the C-In_2S_3 nanosheets showed excellent stability during the catalysis process. After five consecutive cycling experiments, its catalytic performance did not show a significant decrease, and the structure and composition of the photocatalyst remained relatively stable. This finding provides strong support for the

https://doi.org/10.1021/acsomega.4c09487
ACS Omega 2025, 10, 8793−8815

long-term stability and sustainability of C-In_2S_3 nanosheets in practical applications.

5.3. Defect Engineering. Defect engineering can adjust the electronic structure and band configuration of photocatalysts, thereby precisely regulating their light absorption capacity, carrier concentration, and carrier redox characteristics.[109] Furthermore, lattice distortions arising from surface or subsurface defects not only bolster the stability of the photocatalyst but also introduce numerous active sites conducive to CO_2 adsorption and activation. In theory, several types of point defects exist in photocatalysts, including interstitial type, antisite type, and vacancies with variable defect state charges. These defects are usually accompanied by charge compensation and atomic conservation. However, current studies have mainly focused on the vacancies themselves, especially those in nonstoichiometric compounds, which are often reported to be used for solar energy conversion applications.Yang et al.[110] synthesized S-vacancy-rich $CdIn_2S_4$ (VS-$CdIn_2S_4$) by introducing S-vacancies into $CdIn_2S_4$ materials via a unique low-temperature plasma enhancement technique. These S vacancies not only effectively capture photogenerated electrons and provide more active sites, but also form new defect energy levels, which in turn promote the transport of photogenerated carriers, thus significantly enhancing the photocatalytic performance of the material. In the inverse water−gas shift reaction, the CO generation rate of VS-$CdIn_2S_4$ was as high as 103.6 $\mu mol \cdot g^{-1}\ h^{-1}$, which was significantly better than that of the unmodified $CdIn_2S_4$ (31.36 $\mu mol \cdot g^{-1}\ h^{-1}$), showing high activity and stability. By defect engineering, not only the light absorption of the material was increased, but also the charge separation was improved, and this dual improvement led to the excellent CO generation rate. Similarly, the presence of sulfur vacancies on the surface of leafy $CuInS_2$ prepared by Xie et al.[111] facilitated the separation of photogenerated carriers and improved CO_2 adsorption, thus enhancing the efficiency of photothermal catalytic reduction of CO_2.

Metal vacancies are a commonly used method of defect modification. Liao et al.[112] designed a V_{Cu}-$CuInS_2$/MXene heterostructure through in situ hydrothermal synthesis. DFT calculations and XPS showed that Cu vacancies could enhance the interactions between the heterojunctions, promoting the photogenerated charge separation, and increase the charge density of the Ti atoms.This localized electron aggregation facilitates the enhancement of the localized surface plasmon resonance (LSPR) effect, which will further increase the selectivity of the C_2 product. Due to the synergistic effect of Cu vacancies and plasmonic MXene, VCu-$CuInS_2$/MXene obtained excellent CO_2 reduction activity under full-spectrum radiation with an acetate precipitation rate of 250 $\mu mol \cdot g^{-1}\ h^{-1}$ and a product selectivity of up to 97.5%, which is higher than that of V_{Cu}-$CuInS_2$ and $CuInS_2$/MXene, respectively. MXene by a factor of 38.8 and 3.3, respectively. He et al.[113] investigated the photocatalytic CO_2 reduction performance of 3D hierarchical $ZnIn_2S_4$ nanosheets with abundant Zn vacancies (V_{Zn}), and the results showed that V_{Zn} helps to reduce the carrier transport activation energy and promotes the activation and conversion of CO_2 and its intermediates.

Wang et al.[114] constructed a multidimensional composite system in order to further explain the internal relationship between defect structure and properties in composite materials. Fine-control of V_{Zn} concentration in $ZnIn_2S_4$ was achieved by adjusting the hydrothermal reaction temperature (poor-V_{Zn} ZIS (pZIS) and rich-V_{Zn} ZIS (rZIS)). It was found that rZIS samples showed a more open layered flower bulb structure with a clearer edge profile and larger pore volume, which is conducive to the exposure of more surface defects (Figure 10). XRD analysis shows that the characteristic diffraction peak intensity of rZIS sample at 21.2° is higher than that of pZIS sample, which may be closely related to the presence of V_{Zn}. Further XPS analysis revealed significant changes in the position of the characteristic peaks of Zn 2p. Specifically, the position of the characteristic peak of Zn 2p in UCN@rZIS/SWNTs is significantly shifted compared with that in UCN@pZIS/SWNTs, which is related to the difference in V_{Zn} concentration. The shift may be due to the change of Zn electronic state caused by the recombination of upconversion nanoparticles (UCN) with different concentrations of V_{Zn}. The different EPR signal intensity also indicated that the concentration of unpaired electrons and V_{Zn} in UCN@pZIS/SWNTs synthesized at 180 °C was significantly lower than that in UCN@rZIS/SWNTs synthesized at 200 °C. The results of photoelectrochemical experiments showed that a higher concentration of V_{Zn} contributes to the improvement of the separation efficiency of photogenerated carriers due to the construction of UCN@ZIS heterojunctions as well as the diversified charge transfer channels provided by SWNTs. Specifically, when ZIS and UCN were photoexcited, valence band electrons jumped to the conduction band. In the UCN@ZIS heterostructure, electrons were transferred from the conduction band of ZIS to the conduction band of UCN, which prolonged the complexation time of the photogenerated carriers, reduced the reduction potential, and enhanced the CO_2 adsorption capacity and the generation of CO and CH_4. In addition, the V_{Zn} formed at high temperature can further enhance the bonding at the interface between UCN and ZIS, increase the charge density near the receptor center at the complex interface, and lower the activation energy barrier of the reaction system, thus promoting the photocatalytic reduction of CO_2.The UCN@rZIS/SWNTs composites, under the synergistic effect of the active sites on the surface of V_{Zn}, UCN, and the charge transfer channels, showed that the yields of CO and CH_4 reached 33.7 $\mu mol\ g^{-1}$ and 39.8 $\mu mol\ g^{-1}$, respectively, and the selectivity of CH_4 reached 54.1%.

5.4. Co-Catalyst Modification. The introduction of a co-catalyst into a photocatalyst not only effectively promotes electron transfer through the construction of Schottky barriers, thereby improving carrier separation, but also supplements the formation of active sites for the reaction, thereby increasing the adsorption of CO_2 and the stability of the intermediates in the photoreaction. Ideal candidates for co-catalysts include metalloelectrics, alloys, carbon materials and metal oxides/sulfides.[115]

Carbon quantum dots (CQDs) exhibit excellent conductivity and are considered as an ideal co-catalyst. Under the condition of matching energy levels, they can also act as a connection bridge between semiconductors, thereby facilitating the charge separation process. Bi et al.[116] constructed a $CuInS_2$/C/TiO_2 multistage tandem heterostructure using CQDs and C comodified TiO_2 (C/T) as a substrate, and $CuInS_2$ was tightly coated on the surface of a single C/T particle. Given the significant influence of multiple electron transfer behaviors on the activity and selectivity of photocatalytic CO_2 conversion, the important role played by the co-catalysts cannot be ignored. As shown by the in situ

https://doi.org/10.1021/acsomega.4c09487
ACS Omega 2025, 10, 8793−8815

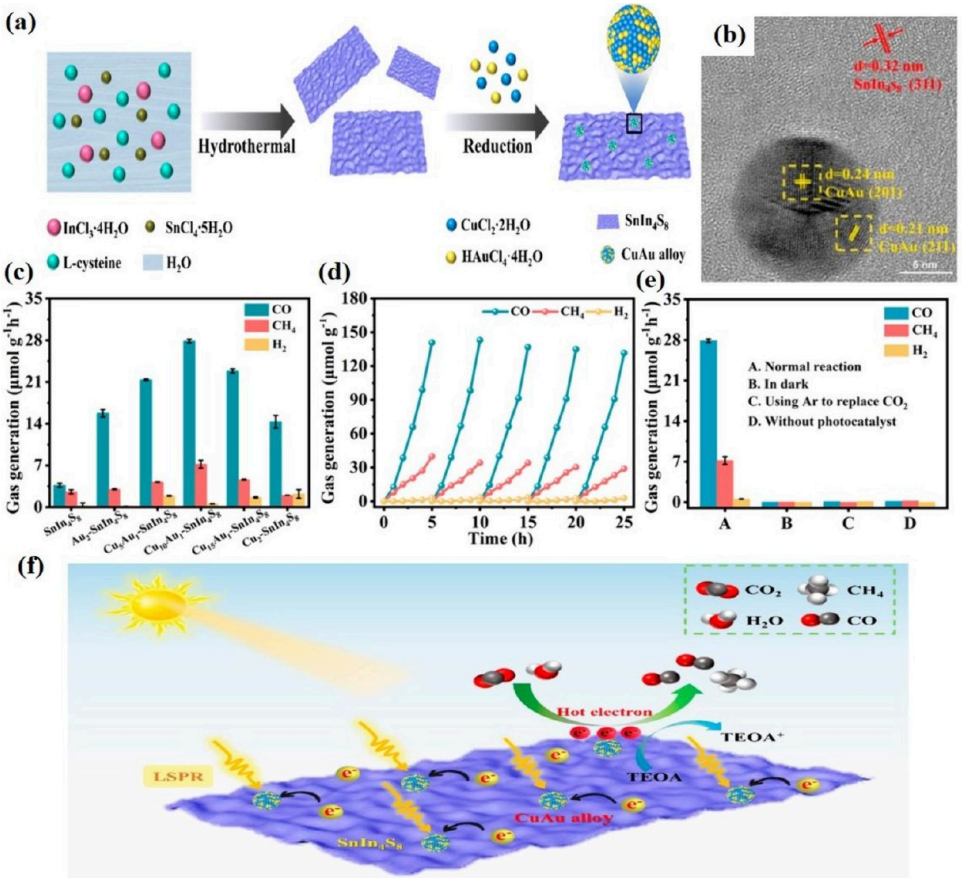

Figure 11. (a) Synthesis roadmap and (b) HRTEM image of $Cu_{10}Au_1$-$SnIn_4S_8$, (c) yield of CO, CH_4 and H_2, (d) stability testing of $Cu_{10}Au_1$-$SnIn_4S_8$, (e) comparison of photocatalytic CO_2 reduction performance under different conditions, (f) schematic diagram of CuAu-$SnIn_4S_8$ photocatalytic reduction of CO_2. Reprinted with permission from ref 117.

characterization and DFT simulation results, the CQDs not only acted as a co-catalyst, but also acted as a bridge between TiO_2 and $CuInS_2$, which promoted the effective separation and enrichment of photogenerated electron−hole pairs, and effectively avoided the complexation of photogenerated carriers. Under the optimal conditions, the CO yield of CIS/C/T can reach 7.73 μmol·g^{-1} h^{-1}, which is about 3.16 times higher than that of C/T. Unlike the $CuInS_2$/C/TiO_2 heterojunction, the CuAu-$SnIn_4S_8$ achieves higher light absorption efficiency by means of an alloy-co-catalyst. The CuAu alloy nanoparticles are round and uniform in size, about 8 nm, and are relatively uniformly loaded on the $SnIn_4S_8$ surface (Figure 11).[117] Throughout the photocatalytic process, photoexcited electrons are promoted from the VB of $SnIn_4S_8$ to its CB, resulting in the creation of numerous holes within the VB and the generation of photoinduced electron−hole pairs. These photoexcited electrons are subsequently transferred swiftly to CuAu alloy nanoparticles, which possess unique LSPR properties facilitating their capture. Ultimately, the electrons accumulate on the CuAu alloy surface and engage in a reaction with CO_2, yielding CO and CH_4. The CuAu-$SnIn_4S_8$ photocatalyst, after optimization, demonstrated a CO generation rate of 27.87 μmol·g^{-1} h^{-1} and a CH_4 generation rate of 7.21 μmol·g^{-1} h^{-1}, which are 7.6 and 2.5 times greater than those of $SnIn_4S_8$, respectively. Additionally, $Cu_{10}Au_1$-$SnIn_4S_8$ exhibited exceptional photocatalytic stability. Following five cycles of testing, it retained significant durability over 25 h, indicating that the structure and morphology of the $Cu_{10}Au_1$-$SnIn_4S_8$ photocatalyst were well-preserved. Controlled experiments conducted under dark conditions and in an Ar atmosphere confirmed that the structure and morphology of the $Cu_{10}Au_1$-$SnIn_4S_8$ catalyst remained stable, making it suitable for photocatalytic CO_2 reduction. This research presents a novel approach to designing alloy co-catalyst-modified metal sulfides for photocatalytic applications.

In addition, noble metals, such as Pt, Ag, Pd, Rh, and Au, have been used as co-catalysts for photocatalytic CO_2 reduction, which can effectively capture and transfer electrons, adsorb and activate CO_2 molecules, thus promoting the generation of CO and CH_4, and decreasing the competition with the hydrogen-extraction reaction (HER). Ma et al.[99] used 1 wt % Pt nanoparticles as co-catalysts for in situ photo deposition. It not only improved the selectivity of the CO_2 reduction reaction, but also effectively captured and transferred electrons, providing active sites to promote the reaction. The yield of CH_4 reached 0.41 μmol·cm^{-2} h^{-1} and that of CO was as high as 1.03 μmol·cm^{-2} h^{-1}. It is worth noting that, although the noble metal co-catalysts showed significant advantages in photocatalytic CO_2 reduction, their high cost is still a key factor restricting their wide application. Therefore, future research should be devoted to the development of low-cost and high-activity alternative materials to promote the practical application of photocatalytic CO_2 reduction technology.

https://doi.org/10.1021/acsomega.4c09487
ACS Omega 2025, 10, 8793−8815

6. CONCLUSION AND PERSPECTIVE

In-based sulfides have demonstrated significant research value in the fields of visible light catalyzed decomposition of aqueous hydrogen, CO_2 reduction, pollutant and antibiotic degradation, organic photoenergy conversion and biological nitrogen fixation due to their narrow bandgap, suitable energy bandgap, and ease of preparation and recycling. In-based metal sulfides have shown excellent catalytic performance as photocatalysts in CO_2 reduction reactions, and their main advantages include strong light absorption, excellent electrical conductivity and chemical stability. In this paper, the role of In-based metal sulfides in photocatalytic CO_2 reduction is reviewed, and their research progress and optimization strategies are discussed. The main structural features, synthetic methods and modification strategies of In-based metal sulfides are introduced, focusing on the effects of heterogeneous structure building, elemental doping, defect engineering and co-catalyst modification on the enhancement of photocatalytic performance. By continuously optimizing the material structure, improving the synthesis method and enhancing the stability and efficiency of the catalysts, In-based photocatalysts are expected to achieve greater breakthroughs in the field of CO_2 reduction and provide practical solutions to tackle global warming and energy crisis. Future research on In-based sulfide photocatalytic materials can focus on the following aspects.

(1) Investigating the photocatalytic mechanism: Currently, the mechanism underlying the photocatalytic reduction of CO_2 remains elusive, and the precise localization of catalytic sites within In-based bimetallic sulfides during the reaction process is still unclear. This significant knowledge gap significantly impedes the progress in developing and synthesizing highly efficient catalysts. To address this challenge, advanced in situ characterization techniques, including in situ XPS, in situ XRD, and in situ XANES spectroscopy, can be employed to monitor the real-time changes in the chemical structure and valence states of the catalyst. These techniques provide a robust foundation for inferring the reaction pathway and elucidating the photocatalytic mechanism.

(2) Optimising the design of synthetic methods. The morphological abundance of In-based metal sulfides is still insufficient, and there is still a huge development space waiting to be explored. From a long-term perspective, the practical application of photocatalytic CO_2 reduction technology puts forward the more stringent standards for the structure of catalysts, while also needing to take into account the yield and cost of catalysts. Especially in the large-scale production process, it is particularly difficult to control the dispersion and morphology of the catalyst, which are precisely the key factors affecting the catalyst performance. At the same time, indium is both rare and expensive, hindering the path to future industrialization. It is necessary to prepare indium matrix composites with other non-noble metals (e.g., Fe and Cu) or nonmetals (e.g., S). Therefore, making full use of the compositional advantages of indium-based metal sulfides with precise design and adjustment is expected to achieve targeted and highly selective product formation. In addition, theoretical calculations need to be introduced to study the mechanism of improving photocatalytic activity at the molecular level when designing In-based photocatalysts. In future studies, DFT simulations and experiments are needed to reveal the relationship between the establishment of microstructures and the catalytic activity of photocatalysts.

(3) Achieving industrialization and industrialization. The current research on photocatalytic technology is mainly focused on the laboratory level, while there is still a lack of relevant research involving large-scale photocatalytic reactors and long flux reactions. Therefore, efforts should be devoted to the development of a new catalyst with the ability of large-scale preparation and tunable morphology, size and structure from both the experimental and industrial application dimensions, so as to effectively reduce the preparation cost. In view of this, the development of efficient indium-based metal sulfide catalysts has become an urgent task, and a cost-optimized method for their mass production needs to be explored.

(4) Reasonable design of the reactor structure to provide the excellent reaction environment for catalyst reaction. The reactor material with better light transmission and stability is used, and the internal flow field and temperature field distribution are reasonably designed. It can further raise the activities and cost-effectiveness of utilized catalysts for realistic application, ought to be explored.

(5) Problems such as the cost and toxicity of catalysts hinder the path to future industrialization. Another interesting approach to solve these problems is the use of mono- or dimonoatomic photocatalysts. Finding cheap and stable metallic or nonmetallic atoms, along with a clean synthetic pathway, is one way to address the future commercialization of photocatalytic CO_2 reduction.

AUTHOR INFORMATION

Corresponding Author

Qian Su − *Department of Chemistry and Chemical & Environmental Engineering, Weifang University, Weifang 261061, China;* orcid.org/0000-0002-8750-5268; Email: 20220033@wfu.edu.cn

Author

Hongyan Zhang − *Department of Chemistry and Chemical & Environmental Engineering, Weifang University, Weifang 261061, China*

Complete contact information is available at: https://pubs.acs.org/10.1021/acsomega.4c09487

Author Contributions

Hongyan Zhang: Writing and revising manuscript, Conceptualization, Methodology, Software, Investigation, Writing-original draft. **Qian Su:** Funding, Acquisition, Supervision, Methodology, Validation, Formal analysis, Visualization. All authors have read and agreed to the published version of the manuscript.

Notes

The authors declare no competing financial interest.

ACKNOWLEDGMENTS

Financial support for carrying out this work was provided by the Doctoral Research Foundation of Weifang University (2022BS13).

https://doi.org/10.1021/acsomega.4c09487
ACS Omega 2025, 10, 8793−8815

REFERENCES

(1) Zhang, W. J.; Ma, D.; Pérez-Ramírez, J.; et al. Recent Progress in Materials Exploration for Thermocatalytic, Photocatalytic, and Integrated Photothermocatalytic CO_2-to-Fuel Conversion. *Advanced Energy and Sustainability Research* **2022**, *3*, 2100169.

(2) Rehman, A.; Nazir, G.; Rhee, K. Y.; et al. Electrocatalytic and photocatalytic sustainable conversion of carbon dioxide to value-added chemicals: State-of-the-art progress, challenges, and future directions. *Journal of Environmental Chemical Engineering* **2022**, *10*, 108219.

(3) Jiang, J. W.; Wang, X. F.; Xu, Q. J.; et al. Understanding dual-vacancy heterojunction for boosting photocatalytic CO_2 reduction with highly selective conversion to CH_4. *Applied Catalysis B: Environmental* **2022**, *316*, 121679.

(4) Sadanandan, A. M.; Yang, J. H.; Devtade, V.; et al. Carbon nitride based nanoarchitectonics for nature-inspired photocatalytic CO_2 reduction. *Prog. Mater. Sci.* **2024**, *142*, 101242.

(5) Huo, Y.; Zhang, P.; Chi, J. J.; et al. Surface Functionalization and Defect Construction of SnO_2 with Amine Group for Enhanced Visible-Light-Driven Photocatalytic CO_2 Reduction. *Adv. Energy Mater.* **2024**, *14*, 2304282.

(6) Liu, X.; Wu, Y. H.; Li, Y. D.; et al. MOF-on-MOF-derived $CuO@In_2O_3$ s-scheme heterojunction with core-shell structure for efficient photocatalytic CO_2 reduction. *Chemical Engineering Journal* **2024**, *485*, 149855.

(7) Ikreedeegh, R. R.; Tahir, M. A critical review in recent developments of metal-organic-frameworks (MOFs) with band engineering alteration for photocatalytic CO_2 reduction to solar fuels. *Journal of CO2 Utilization* **2021**, *43*, 101381.

(8) Kumar, A.; Khosla, A.; Sharma, S. K.; et al. A review on S-scheme and dual S-scheme heterojunctions for photocatalytic hydrogen evolution, water detoxification and CO_2 reduction. *Fuel* **2023**, *333*, 126267.

(9) Inoue, T.; Fujishima, A.; Konishi, S.; et al. Photoelectrocatalytic reduction of carbon dioxide in aqueous suspensions of semiconductor powders. *Nature* **1979**, *277*, 637−638.

(10) Khan, H.; Shah, M. U. H. Modification strategies of TiO_2 based photocatalysts for enhanced visible light activity and energy storage ability: A review. *Journal of Environmental Chemical Engineering* **2023**, *11*, 111532.

(11) Jin, Y. L.; Tang, W. W.; Wang, J. Y. Construction of biomass derived carbon quantum dots modified TiO_2 photocatalysts with superior photocatalytic activity for methylene blue degradation. *J. Alloys Compd.* **2023**, *932*, 167627.

(12) Moridon, S. N. F.; Arifin, K.; Yunus, R. M.; et al. Photocatalytic water splitting performance of TiO_2 sensitized by metal chalcogenides: A review. *Ceram. Int.* **2022**, *48*, 5892−5907.

(13) Zhu, B. C.; Hong, X. Y.; Tang, L. Y.; et al. Enhanced Photocatalytic CO_2 Reduction over 2D/1D $BiOBr_{0.5}Cl_{0.5}/WO_3$ S-Scheme Heterostructure. *Acta Physico-Chimica Sinica* **2021**, *38*, 2111008.

(14) Ahmadi, M.; Alavi, S. M.; Larimi, A.; et al. Highly active platinum decorated $BiVO_4$ nanosheet/TiO_2 nanobelt heterojunction for photocatalytic CO_2 reduction. *Surfaces and Interfaces* **2024**, *45*, 103908.

(15) Yan, Y. K.; Wang, Y.; Zhang, Z. X.; et al. Doping Sn^{4+} ionized cocatalyst in CdSe/S colloidal crystal for promoting photocatalytic CO_2 reduction under visible light. *Chemical Engineering Journal* **2023**, *468*, 143639.

(16) Pei, L.; Wang, X. S.; Zhu, H.; et al. Photothermal Effect- and Interfacial Chemical Bond-Modulated NiO_x/Ta_3N_5 Heterojunction for Efficient CO_2 Photoreduction. *ACS Appl. Mater. Interfaces* **2023**, *15*, 51300−51308.

(17) Sun, Z. X.; Wang, H. Q.; Wu, Z. B. A.; et al. g-C_3N_4 based composite photocatalysts for photocatalytic CO_2 reduction. *Catal. Today* **2018**, *300*, 160−172.

(18) Cui, L. K.; Hu, L. Q.; Shen, Q. Q.; et al. Three-dimensional porous Cu_2O with dendrite for efficient photocatalytic reduction of CO_2 under visible light. *Appl. Surf. Sci.* **2022**, *581*, 152343.

(19) Mo, Z.; Zhu, X. W.; Jiang, Z. F.; et al. Porous nitrogen-rich g-C_3N_4 nanotubes for efficient photocatalytic CO_2 reduction. *Appl. Catal., B* **2019**, *256*, 117854.

(20) Zhan, H.; Zhou, R.; Liu, K.; Ma, Z.; Wang, P.; Zhan, S.; Zhou, Q.; et al. Progress and challenges of photocatalytic reduction of CO_2 with g-C_3N_4-based photocatalysts in the context of carbon neutrality. *Science China Materials* **2024**, *67*, 1740−1764.

(21) Li, Y. X.; Su, W. L.; Wang, X. Y.; et al. In situ topotactic formation of an inorganic intergrowth bulk NiS/FeS@MgFe-LDH heterojunction to simulate CODH for the photocatalytic reduction of CO_2. *Nanoscale* **2024**, *16*, 5776−5785.

(22) Li, S. T.; Zhong, K.; Yang, J. M.; et al. C-S bonds mediated rapid charge transfer in hm-C_4N_3/CdS heterostructure for efficient photocatalytic CO_2 reduction. *J. Colloid Interface Sci.* **2025**, *684*, 300−308.

(23) Gao, X. W.; Li, L. X.; Zhao, Z. W.; et al. Sulfur vacancy-rich ZnS on ordered microporous carbon frameworks for efficient photocatalytic CO_2 reduction. *Applied Catalysis B: Environment and Energy* **2025**, *364*, 124835.

(24) Wang, J. Y.; Zhang, H. Y.; Nian, Y.; et al. Disruption Symmetric Crystal Structure Favoring Photocatalytic CO_2 Reduction: Reduced *COOH Formation Energy Barrier on Al Doped CuS/TiO_2. *Adv. Funct. Mater.* **2024**, *34*, 2406549.

(25) Liu, Z. D.; Chang, X. Q.; Shi, Y. N.; et al. Synergistic effects of $Cu_7S_4@Cu_2O$ core-shell photocatalyst and S-scheme heterojunction in photocatalytic CO_2 reduction. *J. Alloys Compd.* **2025**, *1010*, 177572.

(26) Wang, Y.; Lin, Y. H.; Zha, F. J.; et al. Heterophase junction engineering: Enhanced photo-thermal synergistic catalytic performance of CO_2 reduction over 1T/2H-MoS_2. *J. Colloid Interface Sci.* **2023**, *652*, 936−944.

(27) Fatima, T.; Husain, S.; Narang, J.; et al. Novel tungsten disulfide (WS_2) nanosheets for photocatalytic degradation and electrochemical detection of pharmaceutical pollutants. *Journal of Water Process Engineering* **2022**, *47*, 102717.

(28) Zhang, S. S.; Ou, X. Y.; Xiang, Q.; et al. Research progress in metal sulfides for photocatalysis: From activity to stability. *Chemosphere* **2022**, *303*, 135085.

(29) Zhao, Z. Y.; Cao, Y. C.; Yi, J.; et al. Band-Edge Electronic Structure of ß-In_2S_3: The Role of s or p Orbitals of Atoms at Different Lattice Positions. *ChemPhysChem* **2012**, *13*, 1551−1556.

(30) Nie, Y.; Bo, T. T.; Zhou, W.; et al. Understanding the role of Zn vacancy induced by sulfhydryl coordination for photocatalytic CO_2 reduction on $ZnIn_2S_4$. *Journal of Materials Chemistry A* **2023**, *11*, 1793.

(31) Zhu, C. S.; Li, J. Y.; Chai, Y. K.; et al. Synergistic Cr(VI) Reduction and Chloramphenicol Degradation by the Visible-Light-Induced Photocatalysis of $CuInS_2$: Performance and Reaction Mechanism. *Frontiers in Chemistry* **2022**, *10*, 964008.

(32) Liao, C.; He, Z. Z.; Wang, F.; et al. Anti-Site Defect-Induced Cascaded Sub-Band Transition in $CuInS_2$ Enables Infrared Light-Driven CO_2 Reduction. *ACS Nano* **2024**, *18* (52), 35480−35489.

(33) Zhang, H. B.; Wang, Z. L.; Zhang, J. F.; et al. Metal-sulfide-based heterojunction photocatalysts: Principles, impact, applications, and in-situ characterization. *Chinese Journal of Catalysis* **2023**, *49*, 42−67.

(34) Oh, V. B. Y.; Ng, S. F.; Ong, W. J.; et al. Shining light on $ZnIn_2S_4$ photocatalysts: Promotional effects of surface and heterostructure engineering toward artificial photosynthesis. *Ecomat* **2022**, *4*, No. e12204.

(35) Tai, X. S.; Yan, X. H.; Wang, L. H. Synthesis, Structural Characterization, Hirschfeld Surface Analysis, Density Functional Theory, and Photocatalytic CO_2 Reduction Activity of a New Ca(II) Complex with a Bis-Schiff Base Ligand. *Molecules* **2024**, *29*, 1047.

(36) Albero, J.; Peng, Y.; Garcia, H. Photocatalytic CO_2 reduction to C_{2+} products. *ACS Catal.* **2020**, *10*, 5734−5749.

(37) Hu, X.; Guo, R. T.; Chen, X.; et al. Bismuth-based Z-scheme structure for photocatalytic CO_2 reduction: A review. *Journal of Environmental Chemical Engineering* **2022**, *10*, 108582.

https://doi.org/10.1021/acsomega.4c09487
ACS Omega 2025, 10, 8793−8815

(38) Sabbah, A.; Shown, I.; Qorbani, M.; et al. Boosting photocatalytic CO_2 reduction in a $ZnS/ZnIn_2S_4$ heterostructure through strain-induced direct Z-scheme and a mechanistic study of molecular CO_2 interaction thereon. *Nano Energy* **2022**, *93*, 106809.
(39) Li, L. L.; Ma, D. K.; Xu, Q. L.; et al. Constructing hierarchical $ZnIn_2S_4/g\text{-}C_3N_4$ S-scheme heterojunction for boosted CO_2 photoreduction performance. *Chemical Engineering Journal* **2022**, *437*, 135153.
(40) Zhu, X. L.; Zong, H. B.; Pérez, C. J.; et al. Supercharged CO_2 Photothermal catalytic Methanation: High Conversion, Rate, and Selectivity. *Angew. Chem., Int. Ed.* **2023**, *62*, No. e202218694.
(41) Su, Q.; Guo, Q. J.; Wang, H. Q.; et al. Research progress of MOF-based materials in the photocatalytic CO_2 reduction. *Carbon Resources Conversion* **2024**, *7*, 100211.
(42) Tai, X. S.; Yan, X. H.; Wang, L. H. Synthesis, Structural Characterization, Hirschfeld Surface Analysis, Density Functional Theory, and Photocatalytic CO_2 Reduction Activity of a New Ca(II) Complex with a Bis-Schiff Base Ligand. *Molecules* **2024**, *29*, 1047.
(43) Jiang, H. P.; Xu, M. Y.; Zhao, X. X.; et al. Construction of a $ZnIn_2S_4$/Au/CdS Tandem Heterojunction for Highly Efficient CO_2 Photoreduction. *Inorg. Chem.* **2022**, *61*, 11207−11217.
(44) Maruska, H. P.; Ghosh, A. K. Photocatalytic decomposition of water at semiconductor electrodes. *Sol. Energy* **1978**, *20*, 443−458.
(45) Yuan, Z. M.; Zhu, X. L.; Gao, X. Q.; et al. Enhancing photocatalytic CO_2 reduction with TiO_2-based materials: Strategies, mechanisms, challenges, and perspectives. *Environ. Sci. Ecotechnol.* **2024**, *20*, 100368.
(46) Ochedi, F. O.; Liu, D.; Yu, J.; et al. Photocatalytic, electrocatalytic and photoelectrocatalytic conversion of carbon dioxide: a review. *Environmental Chemistry Letters* **2021**, *19*, 941−967.
(47) Mishra, S. R.; Gadore, V.; Ahmaruzzaman, M. Recent advances in In_2S_3-based photocatalysts for catalytic reduction of CO_2. *Chemical Physics Impact.* **2023**, *7*, 100324.
(48) Miao, Y. F.; Guo, R. T.; Gu, J. W.; et al. Fabrication of β-In_2S_3/NiAl-LDH heterojunction photocatalyst with enhanced separation of charge carriers for efficient CO_2 photocatalytic reduction. *Appl. Surf. Sci.* **2020**, *527*, 146792.
(49) Alhamzani, A. G.; Yousef, T. A.; Abou-Krisha, M. M.; Kumar, K. Y.; Prashanth, M.K.; Parashuram, L.; Hun Jeon, B.; Raghu, M.S.; et al. Fabrication of layered In_2S_3/WS_2 heterostructure for enhanced and efficient photocatalytic CO_2 reduction and various paraben degradation in water. *Chemosphere* **2023**, *322*, 138235.
(50) Yan, D. H.; Wan, Z. Y.; Wang, K.; et al. In_2O_3/In_2S_3 Heterostructures derived from In-MOFs with enhanced visible light photocatalytic performance for CO_2 reduction. *ChemistrySelect* **2021**, *6*, 2508−2515.
(51) Shen, S.; Guo, P.; Zhao, L.; et al. Insights into photoluminescence property and photocatalytic activity of cubic and rhombohedral $ZnIn_2S_4$. *J. Solid State Chem.* **2011**, *184*, 2250−2256.
(52) Chen, J.; Xin, F.; Yin, X.; et al. Synthesis of hexagonal and cubic $ZnIn_2S_4$ nanosheets for the photocatalytic reduction of CO_2 with methanol. *RSC Adv.* **2015**, *5*, 3833−3839.
(53) Wang, S.; Guan, B. Y.; Lou, X.; et al. Construction of $ZnIn_2S_4$-In_2O_3 hierarchical tubular heterostructures for efficient CO_2 photoreduction. *J. Am. Chem. Soc.* **2018**, *140*, 5037−5040.
(54) Xia, Y.; Cheng, B.; Fan, J. J.; et al. Near-infrared absorbing 2D/3D $ZnIn_2S_4$/N-doped graphene photocatalyst for highly efficient CO_2 capture and photocatalytic reduction. *Science ChinaMaterials* **2020**, *63*, 552−565.
(55) Wang, X.; Guo, Q. J.; Kong, T. T. Tetraethylenepentamine-modified MCM-41/silica gel with hierarchical mesoporous structure for CO_2 capture. *Chemical Engineering Journal* **2015**, *273*, 472−480.
(56) Li, S.; Li, H.; Wang, Y. N.; et al. Mixed-valence bimetallic Ce/Zr-NH_2-UiO-66 modified with $CdIn_2S_4$ to form S-scheme heterojunction for boosting photocatalytic CO_2 reduction. *Sep. Purif. Technol.* **2024**, *333*, 125994.
(57) Yu, H.; Dou, M. H.; Wang, S.; et al. ZIF-8-supported $AgInS_2$ quantum dots for photocatalytic H_2 production by precise location sulfurization. *ACS Appl. Mater. Interfaces* **2023**, *6*, 228−237.
(58) Wang, H. J.; Li, J. Z.; Wan, Y.; et al. Synthesis of $AgInS_2$ QDs-MoS_2/GO composite with enhanced interfacial charge separation for efficient photocatalytic degradation of tetracycline and CO_2 reduction. *J. Alloys Compd.* **2023**, *954*, 170159.
(59) Deng, Y.; Wang, H.; Zhang, Q.; Guo, Y.; Wang, J. Polyethyleneimine coated $AgInS_2$ quantum dots for efficient CO_2 photoreduction to C_2H_6. *Carbon Capture Science & Technology* **2024**, *13*, 100272.
(60) Weng, R. G.; Tian, F.; Yu, Z. D.; et al. Efficient mineralization of TBBPA via an integrated photocatalytic reduction/oxidation process mediated by $MoS_2/SnIn_4S_8$ photocatalyst. *Chemosphere* **2021**, *285*, 131542.
(61) Deng, F.; Lu, X.; Zhao, L.; et al. Facile low-temperature co-precipitation method to synthesize hierarchical network-like $g\text{-}C_3N_4$/$SnIn_4S_8$ with superior photocatalytic performance. *Journal Of Materials Science* **2016**, *51*, 6998−7007.
(62) Deng, F.; Zhong, F.; Zhao, L.; et al. One-step in situ hydrothermal fabrication of octahedral $CdS/SnIn_4S_8$ nano-heterojunction for highly efficient photocatalytic treatment of nitrophenol and real pharmaceutical wastewater. *Journal of Hazardous Materials* **2017**, *340*, 85−95.
(63) Xu, P. F.; Zhang, R. Q.; Gong, J. R.; et al. S-Scheme WO_3/$SnIn_4S_8$ Heterojunction for Water Purification: Enhanced Photocatalytic Performance and Mechanism. *Catalysts* **2023**, *13*, 1450.
(64) Xu, P.; Huang, S.; Liu, M.; et al. Z-Schemed WO_3/rGO/$SnIn_4S_8$ sandwich nanohybrids for efficient visible light photocatalytic water purification. *Catalysts* **2019**, *9*, 187.
(65) Wang, X. F.; Jiang, J. W.; Xu, Q. J.; et al. Understanding inclusive quantum dots hollow CN@CIZS heterojunction for enhanced photocatalytic CO_2 reduction. *Appl. Surf. Sci.* **2022**, *604*, 154601.
(66) Liang, N.; He, Q. Q.; Huang, S. S.; et al. $AgIn_xGa_{1-x}S_2$ solid solution nanocrystals: synthesis, band gap tuning and photocatalytic activity. *CrystEngComm* **2014**, *16*, 10123.
(67) Yuan, Z Q; Xiang, Y; Jian, X $Zn_{0.5}Cd_{0.5}S/MoTe_2$ Z-scheme heterojunction with space-separated oxidation-reduction catalytic sites for photocatalytic CO_2 reduction. *Separation and Purification Technology* **2025**, *359*, 129836.
(68) Zhao, T. W.; Zhang, W. X.; Xiong, J. Y.; et al. Lewis base and metallic sites cooperatively promotes photocatalytic CO_2 reduction in PO_4^{3-}/Ag-TiO_2 hybrids. *Sep. Purif. Technol.* **2025**, *360*, 130849.
(69) Bian, Y. Q.; He, H. W.; Dawson, G.; et al. $In_2O_3/Bi_{19}Br_3S_{27}$ S-scheme heterojunction with enhanced photocatalytic CO_2 reduction. *Sci. China Mater.* **2024**, *67*, 514−523.
(70) Meng, J. Z.; Wang, K. W.; Wang, Y.; et al. Bismuth clusters pinned on TiO_2 porous nanowires boosting charge transfer for CO_2 photoreduction to CH_4. *Nano Research* **2024**, *17*, 1190−1198.
(71) Jökel, J. L.; Boydas, E. B.; Wellauer, J.; et al. A $Cu^{I}Co^{II}$ cryptate for the visible light-driven reduction of CO_2. *Chemical Science* **2023**, *14*, 12774−12783.
(72) Guo, F.; Li, R. X.; Yang, S. Z.; et al. Designing Heteroatom-Codoped Iron Metal-Organic Framework for Promotional Photoreduction of Carbon Dioxide to Ethylene. *Angew. Chem., Int. Ed.* **2023**, *62*, No. e202216232.
(73) Ma, M. Z.; Huang, Z. A.; Doronkin, D. E.; et al. Ultrahigh surface density of Co-N_2C single-atom-sites for boosting photocatalytic CO_2 reduction to methanol. *Applied Catalysis B: Environmental* **2022**, *300*, 120695.
(74) Liao, A. Z.; Liu, Z. C.; Wei, Y. Q.; et al. Synthesis of Sulfur Vacancy-Bearing $In_2S_3/CuInS_2$ Microflower Heterojunctions via a Template-Assisted Strategy and Cation-Exchange Reaction for Photocatalytic CO_2 Reduction. *Molecules* **2024**, *29*, 3334.
(75) Xia, Y. Z.; Xiao, J. L.; Zhang, J. C.; et al. Construction of a sunflower-like S-scheme $WO_3/ZnIn_2S_4$ heterojunction with spatial charge transfer for enhanced photocatalytic CO_2 reduction. *Fuel* **2025**, *382*, 133779.
(76) Jiang, Y. H.; Peng, Z. Y.; Wu, F. W.; et al. A novel 3D/2D $CdIn_2S_4$ nano-octahedron/ZnO nanosheet heterostructure: facile synthesis, synergistic effect and enhanced tetracycline hydrochloride

https://doi.org/10.1021/acsomega.4c09487
ACS Omega 2025, 10, 8793−8815

photodegradation mechanism. *Dalton Transactions* **2018**, *47*, 8724−8737.
(77) Jiang, W.; Yin, X.; Xin, F.; et al. Preparation of $CdIn_2S_4$ microspheres and application for photocatalytic reduction of carbon dioxide. *Appl. Surf. Sci.* **2014**, *288*, 138−142.
(78) Bhirud, A.; Chaudhari, N.; Nikam, L.; et al. Surfactant tunable hierarchical nanostructures of $CdIn_2S_4$ and their photohydrogen production under solar light. *Int. J. Hydrogen Energy* **2011**, *36*, 11628−11639.
(79) Bai, X.; Li, J. Photocatalytic hydrogen generation over porous $ZnIn_2S_4$ microspheres synthesized via a CPBr-assisted hydrothermal method. *Mater. Res. Bull.* **2011**, *46*, 1028−1034.
(80) Du, C.; Zhang, Q.; Lin, Z.; et al. Half-unit-cell $ZnIn_2S_4$ monolayer with sulfur vacancies for photocatalytic hydrogen evolution. *Applied Catalysis B: Environmental* **2019**, *248*, 193−201.
(81) Gou, X.; Cheng, F.; Shi, Y.; et al. Shape-controlled synthesis of ternary chalcogenide $ZnIn_2S_4$ and $CuIn(S,Se)_2$ nano-/microstructures via facile solution route. *Journal of the American chemical society* **2006**, *128*, 7222−7229.
(82) Song, Y. L.; Zhang, H.; Li, Z. Y.; et al. Study on optimum preparation conditions of $ZnIn_2S_4$ to effectively reduce Cr(VI) under visible light radiation. *Catalysts* **2022**, *12*, 1429.
(83) Compton, J. S.; Peterson, C. A.; Dervishogullari, D.; et al. Spray pyrolysis as a combinatorial method for the generation of photocatalyst libraries. *ACS Comb. Sci.* **2019**, *21*, 489−499.
(84) Workie, A. B.; Workie, H. S.; Shih, S. J. An comprehensive review on the spray pyrolysis technique: Historical context, operational factors, classifications, and product applications. *Journal of Analytical and Applied Pyrolysis* **2023**, *170*, 105915.
(85) Tiss, B.; Benfraj, M.; Bouguila, N.; et al. The effect of vacuum and air annealing in the physical characteristics and photocatalytic efficiency of In_2S_3: Ag thin films produced by spray pyrolysis. *Mater. Chem. Phys.* **2021**, *270*, 124838.
(86) Li, M. T.; Su, J. Z.; Guo, L. J. Preparation and characterization of $ZnIn_2S_4$ thin films deposited by spray pyrolysis for hydrogen production. *International Association for Hydrogen Energy* **2008**, *33*, 2891−2896.
(87) Enesca, A.; Yamaguchi, Y. C.; Terashima, C.; et al. Enhanced UV-Vis photocatalytic performance of the $CuInS_2/TiO_2/SnO_2$ hetero-structure for air decontamination. *J. Catal.* **2017**, *350*, 174−181.
(88) Basaleh, A. S.; Amin, M. S.; Mahmoud, M. H. H. $ZnIn_2S_4$/g-C_3N_4 Nanocomposite for Proficient Elimination of Hg (II) under Visible Light. *Journal of Inorganic and Organometallic Polymers and Materials* **2021**, *31*, 3829−3841.
(89) Ma, M. T.; Lin, Y. M.; Maheskumar, V.; et al. A highly efficient (Mo, N) codoped $ZnIn_2S_4$/g-C_3N_4 Z-scheme photocatalyst for the degradation of methylene blue. *Appl. Surf. Sci.* **2022**, *585*, 152607.
(90) Chen, T. T.; Zhou, M.; Zhang, Z. Q.; et al. Reinforcing flower-like $ZnIn_2S_4$ via interfacial charge separation to boost CO_2 photoreduction. *Chem. Eng. Sci.* **2024**, *285*, 119546.
(91) Assaker, I. B.; Gannouni, M.; Naceur, J. B.; Almessiere, M. A.; Al-Otaibi, A. L.; Ghrib, T.; Shen, S.; Chtourou, R.; et al. Electrodeposited $ZnIn_2S_4$ onto TiO_2 thin films for semiconductor-sensitized photocatalytic and photoelectrochemical applications. *Appl. Surf. Sci.* **2015**, *351*, 927−934.
(92) Wang, L. J.; Li, Q.; Song, J. P.; et al. Construction of hierarchical $FeIn_2S_4$/BiOBr S-scheme heterojunction with enhanced visible-light photocatalytic performance for antibiotics degradation. *Advanced Powder Technology* **2022**, *33*, 103859.
(93) Rahman, A.; Khan, F.; Jennings, J. R.; et al. Microwave-assisted synthesis of ZnS@$CuIn_xS_y$ for photocatalytic degradation of coloured and non-coloured pollutants. *Sci. Rep.* **2024**, *14*, 16155.
(94) Wang, S. B.; Guan, B. Y.; Lu, Y.; et al. Formation of Hierarchical In_2S_3-$CdIn_2S_4$ Heterostructured Nanotubes for Efficient and Stable Visible Light CO_2 Reduction. *J. Am. Chem. Soc.* **2017**, *139*, 17305−17308.
(95) Yang, J. M.; Yang, Z. R.; Yang, K. F.; et al. Indium-based ternary metal sulfide for photocatalytic CO_2 reduction application. *Chinese Journal of Catalysis* **2023**, *44*, 67−95.
(96) Huang, L. J.; Li, B. F.; Su, B.; et al. Fabrication of hierarchical Co_3O_4@$CdIn_2S_4$ p-n heterojunction photocatalysts for improved CO_2 reduction with visible light. *Journal of Materials Chemistry A* **2020**, *8*, 7177−7183.
(97) Tan, J.; Yu, M. S.; Cai, Z. Z.; et al. MOF-derived synthesis of MnS/In_2S_3 p-n heterojunctions with hierarchical structures for efficient photocatalytic CO_2 reduction. *J. Colloid Interface Sci.* **2021**, *588*, 547−556.
(98) Chang, S. Q.; Feng, Y.; Zhao, Y. C.; et al. Fabrication of p-n heterostructured photocatalysts with triazinebased covalent organic framework and $CuInS_2$ for high-Efficiency CO_2 reduction. *ACS Applied Materials&Interfaces* **2024**, *16*, 13839−13848.
(99) Ma, Y. Y.; Zhang, Z. M.; Jiang, X.; et al. Direct Z-scheme Sn-In_2O_3/In_2S_3 heterojunction nanostructures for enhanced photocatalytic CO_2 reduction activity. *Journal of Materials Chemistry C* **2021**, *9*, 3987.
(100) Chen, Q. L.; Wang, S.; Miao, B. J.; et al. Dual p-n Z-scheme heterostructure boosted superior photoreduction CO_2 to CO, CH_4 and C_2H_4 in In_2S_3/MnO_2/BiOCl photocatalyst. *J. Colloid Interface Sci.* **2024**, *663*, 1005−1018.
(101) Zhu, B. C.; Sun, J.; Zhao, Y. Y.; et al. Construction of 2D S-Scheme Heterojunction Photocatalyst. *Adv. Mater.* **2024**, *36*, 2310600.
(102) Zhang, Z. W.; Guo, R. T.; Tang, J. Y.; et al. Fabrication of Bi-BiOCl/$MgIn_2S_4$ heterostructure with step-scheme mechanism for carbon dioxide photoreduction into methane. *Journal of CO2 Utilization* **2021**, *45*, 101453.
(103) Wang, K.; Shao, X. L.; Cheng, Q.; et al. In Situ-Illuminated X-Ray Photoelectron Spectroscopy Investigation of S-Scheme Ta_2O_5/$ZnIn_2S_4$ Core-Shell Hybrid Nanofibers for Highly Efficient Solar-Driven CO_2 Overall Splitting. *Solar RRL* **2022**, *6*, 2200736.
(104) Xiong, R. Z.; Ke, X. X.; Jia, W. F.; et al. Photothermal-coupled solar photocatalytic CO_2 reduction with high efficiency and selectivity on a MoO_{3-x}@$ZnIn_2S_4$ core-shell S-scheme heterojunction. *Journal of Materials Chemistry A* **2023**, *11*, 2178−2190.
(105) Zhou, F. H.; Zhang, Y. L.; Wu, J.; et al. Utilizing Er-doped $ZnIn_2S_4$ for efficient photocatalytic CO_2 conversion. *Applied Catalysis B-Environmental and Energy* **2024**, *341*, 123347.
(106) Yang, W.; Dong, Y.; Wang, Z.; et al. Synthesis, characterization, and photocatalytic activity of stannum-doped $MgIn_2S_4$ microspheres. *J. Alloys Compd.* **2021**, *860*, 158446.
(107) Qin, J.; Zhao, Q.; Zhao, Y.; et al. Metal-free phosphorus-doped $ZnIn_2S_4$ nanosheets for enhanced photocatalytic CO_2 reduction. *J. Phys. Chem. C* **2021**, *125*, 23813−23820.
(108) Wang, L.; Zhao, B. H.; Wang, C. H.; et al. Thermally assisted photocatalytic conversion of CO_2-H_2O to C_2H_4 over carbon doped In_2S_3 nanosheets. *Journal of Materials Chemistry A* **2020**, *8*, 10175−10179.
(109) Shen, M.; Zhang, L. X.; Shi, J. L.; et al. Defect Engineering of Photocatalysts towards Elevated CO_2 Reduction Performance. *ChemSusChem* **2021**, *14*, 2635−3654.
(110) Yang, J. M.; Zhu, X. W.; Yu, Q.; et al. Plasma-induced defect engineering: boosted the reverse water gas shift reaction performance with electron trap. *J. Colloid Interface Sci.* **2020**, *580*, 814−821.
(111) Yang, C. Y.; Shi, J. P.; Wang, Z. S.; et al. One step hydrothermal preparation of leaf-like $CuInS_2$ micro-nano structures on three-dimensional flexible substrate to enhance photothermal catalytic activity. *Appl. Surf. Sci.* **2024**, *649*, 159107.
(112) Liao, C.; Zhou, H. W.; Zhang, S. X.; et al. Copper Vacancy and LSPR-Activated MXene Synergistically Enabling Selective Photoreduction CO_2 to Acetate. *ChemSusChem* **2024**, *17*, No. e202301927.
(113) He, Y.; Rao, H.; Song, K.; et al. 3D hierarchical $ZnIn_2S_4$ nanosheets with rich Zn vacancies boosting photocatalytic CO_2 reduction. *Adv. Funct. Mater.* **2019**, *29*, 1905153.

https://doi.org/10.1021/acsomega.4c09487
ACS Omega 2025, 10, 8793−8815

(114) Wang, H. J.; Li, J. Z.; Wan, Y.; et al. Fabrication of Zn vacancies-tunable ultrathin-g-C_3N_4@$ZnIn_2S_4$/SWNTs composites for enhancing photocatalytic CO_2 reduction. *Appl. Surf. Sci.* **2023**, *613*, 155989.
(115) Zuo, C.; Su, Q.; Yan, X. Y. Research Progress of Co-Catalysts in Photocatalytic CO_2 Reduction: A Review of Developments, Opportunities, and Directions. *Processes* **2023**, *11*, 867.
(116) Bi, W.; Zhang, L.; Jiang, H.; et al. Construction of $CuInS_2$/C/TiO_2 hierarchical tandem heterostructures with optimized CO_2 photoreduction under visible light. *Chemical Engineering Journal* **2022**, *433*, 133679.
(117) Yang, Z. R.; Yang, J. M.; Yang, K. F.; et al. Synergistic Effect in Plasmonic CuAu Alloys as Co-Catalyst on $SnIn_4S_8$ for Boosted Solar-Driven CO_2 Reduction. *Catalysts* **2022**, *12*, 1588.

https://doi.org/10.1021/acsomega.4c09487
ACS Omega 2025, 10, 8793−8815